Final, accepted version
File LockwoodandMcWilliams_2021_F1.doc
submitted to: J. Geophys. Res. 11th May 2021
revised: 24 June 2021
accepted: 26 July 2021

A survey of 25 years' transpolar voltage data from the SuperDARN radar network and the Expanding-Contracting Polar Cap model

Mike Lockwood[1] and Kathryn A. McWilliams[2]

[1] *Department of Meteorology, University of Reading, Earley Gate, Reading, RG6 6BB, UK*

[2] *Institute of Space and Atmospheric Studies, University of Saskatchewan, Saskatoon, Saskatchewan, S7N 5E2, Canada*

Abstract. We use 214410 hourly observations of transpolar voltage, Φ_{PC}, from 25 years' observations by the SuperDARN radars to confirm the central tenet of the Expanding-Contracting Polar Cap model of ionospheric convection that Φ_{PC} responds to both dayside and nightside reconnection voltages (Φ_D and Φ_N). We show Φ_{PC} increases at a fixed level of the nightside auroral electrojet *AL* index with increasingly southward IMF (identifying the well-known effect of Φ_D on Φ_{PC}) but also with increasingly negative AL at a fixed southward IMF (identifying a distinct effect of Φ_N on Φ_{PC}). We also study the variation of Φ_{PC} with time elapsed Δt since the IMF last pointed southward and show low/large values occur when $(-AL)$ is small/large. Lower numbers of radar echoes, n_e, mean that the "map-potential" re-analysis technique used to derive Φ_{PC} is influenced by the model used: we present a sensitivity study of the effect of the threshold of n_e required to avoid this. We show that for any threshold n_e, Φ_{PC} falls to about 15 kV for Δt greater than about 15 hours, indicating any viscous-like voltage Φ_V is considerably smaller than this. It is shown that both Φ_{PC} and $(-AL)$ increase with increased solar wind dynamic pressure p_{SW}, but not as much as the mid-latitude geomagnetic index am. We conclude p_{SW} increases both Φ_D and Φ_N through increasing the magnetic shear across the relevant current sheet but has a larger effect on mid-latitude geomagnetic indices because of the effect of additional energy stored in the tail lobes.

1. Introduction.

This paper studies the Expanding-Contracting Polar Cap (ECPC) model of ionospheric convection excitation (*Cowley and Lockwood*, 1992) using an unprecedentedly large dataset of observations of the transpolar voltage Φ_{PC}, also known as the cross-cap potential difference. The ECPC model predicts that Φ_{PC} at any one instant depends on the reconnection voltage in the cross-tail current sheet Φ_N as well as that at the dayside magnetopause Φ_D.

One specific aim is to re-create two scatter plots from surveys of Φ_{PC} that have been of great importance to our understanding of the excitation of ionospheric polar convection by the solar wind flow, but here using a very much larger dataset of observations. The first of these scatter plots shows the dependence of Φ_{PC} on the northward component B_Z of the Interplanetary Magnetic Field (IMF) in the Geocentric Solar Magnetospheric (GSM) reference frame (*Reiff et al*., 1981; *Cowley*, 1984*; Boyle*, 1997; *Hairston et al*., 1998; *Milan et al.*, 2004; *Liu et al*., 2019). The second scatter plot shows the dependence of Φ_{PC} during northward IMF ($B_Z > 0$) on the time elapsed since the IMF was last southward (*Wygant et al.*, 1983). We also aim to use the large dataset, which covers more than a whole Hale solar magnetic cycle, to extend our understanding of the separate effects of reconnection in the magnetopause and the cross-tail current sheet by comparisons with the behaviour of the AL auroral electrojet index and to investigate the separate effects of solar wind dynamic pressure on Φ_D and Φ_N.

1-i. Transpolar voltage, steady state and non-steady-state convection

Magnetospheric convection (the circulation of plasma and frozen-in magnetic field) is at the heart of our understanding of the response of geomagnetic activity and terrestrial space weather to the transfer of energy from the solar wind into the magnetosphere. Directly-driven geomagnetic responses, historically called "Disturbance Polar-2" or "DP-2", are usually dominated by eastward currents in the afternoon sector polar ionosphere and detected as positive enhancements of the AU auroral electrojet index. DP-2 currents correlate highly with solar wind forcing at short response delays (*Nishida*, 1968a; b; *Lockwood et al.*, 1986; *Etemadi et al*., 1988; *Todd et al.*, 1988). These are driven responses to magnetic reconnection in the dayside magnetopause current sheet which generates open magnetospheric field lines (*Consolini and De Michelis*, 2005; *Finch et al.*, 2008; *Echer et al.*, 2017), the voltage Φ_D being the magnetic flux transfer rate from the closed to open magnetospheric field-line

topology. The open field lines generated are swept into the geomagnetic tail by the solar wind flow where they accumulate, storing energy there. These open field lines in the tail are subsequently re-closed in bursts of reconnection in the cross-tail current sheet, giving the storage-release responses of geomagnetic activity ("DP-1") after a longer lag time than for the DP-2 response (*Baker et al.*, 1983; *McPherron et al.*, 1998; *Klimas et al.*, 1992; 1994; *Finch et al.*, 2008). The DP-1 response is dominated by the effects of the westward auroral electrojet current across midnight in the substorm current wedge and seen as negative perturbations of the *AL* auroral electrojet index. The voltage Φ_N is the magnetic flux transfer rate from the open to the closed magnetospheric field-line topology. The storage-release response is often described in terms of the magnetospheric substorm cycle (e.g., *Baker et al.*, 1997; *McPherron et al.*, 1998). A review of the development of our understanding of the relationship of magnetospheric flux transport, the Dungey convection cycle and substorms has been given by *McPherron* (2020) and a review of the associated energy flow through the magnetosphere has been given by *Lockwood* (2019).

Being at the foot of magnetospheric field lines and, like the magnetosphere, being of high magnetic Reynolds number, the frozen-in flux theorem applies in the polar ionospheric F-region and topside ionosphere. Hence these regions reflect the circulation of frozen-in flux in the magnetosphere (ionospheric convection). However, there is one key difference between the flows in the magnetosphere and in the ionosphere. The magnetosphere is compressible, a fact that the storage-release system depends upon. On the other hand, the ionosphere is incompressible, in the sense that the magnetic field there is constant to within a very small factor, such that even a very large geomagnetic disturbance is only a very small fraction of the intrinsic geomagnetic field (for example, 1000 nT is less than a 2% perturbation). The reason for this is the ionosphere's close proximity to the currents in the Earth's interior that generate the geomagnetic field. This difference means that during substorm growth phases, when energy is accumulating in the near-Earth lobes of the magnetospheric geomagnetic tail because the field there is growing (and to some extent also because the lobes are expanding in cross-sectional area as the tail flares), the ionospheric footprint of the open field lines of the lobes (the open polar caps) must be expanding in area (*Holzer et al.*, 1986; *Lockwood et al.*, 1990; *Lockwood and Cowley*, 1992, *Milan et al*., 2003; 2009; 2012; *Huang et al.*, 2009). *Siscoe and Huang* (1985) showed how expanding "adiaroic" segments polar cap boundaries (meaning "not flowing across", i.e., not mapping to a magnetospheric reconnection site)

would influence the pattern of ionospheric convection. This concept was used by *Cowley and Lockwood* (1992) to show how ionospheric convection is driven by both the generation and destruction of open flux (the "Expanding-Contracting Polar Cap", ECPC model). This is different to the magnetosphere, where flows are driven by the solar wind flow, pressure balance and the magnetohydrodynamic (MHD) curvature force that acts to straighten bent field lines. The ECPC concept is supported by detailed comparisons between theory and observations of how patches of newly-opened flux, generated by magnetopause reconnection bursts, evolve poleward (*Cowley et al.,* 1991a; *Lockwood et al.,* 1993; *McWilliams et al*., 2000; *Throp et al*., 2005; *Lockwood et al.,* 2006). The result of these considerations is that ionospheric convection is not, in general, a straightforward image of the magnetospheric circulation and the two are decoupled by induction effects – changes in the magnetic field between the magnetosphere and the ionosphere which, by Faraday's law, give a curl in the electric field (*Lockwood et al*., 1990; *Lockwood and Cowley*, 1992; *Lockwood and Morley*, 2004). In steady-state, the electric field becomes curl-free and electrostatic potentials do map down magnetic field lines. In addition, in steady state the adiaroic boundaries are not moving. Steady state applies when data are averaged over a long enough timescale; however, theory of substorm growth and expansion predicts that it will not apply to the timescales of a few substorm cycles or less. That is not to say that balanced reconnection events, when dayside and nightside reconnection voltages are approximately equal, do not occur (*DeJong et al.,* 2008, *Lockwood et al*., 2009): these can occur by chance but, probably more often, they occur because changes in the dayside reconnection voltage are sufficiently slow, such that it is never greatly different to the lagged nightside voltage response (*Milan et al*., 2021). Surveys by *Lockwood et al.* (2009) and *Milan et al.* (2021) have looked at the relative occurrence of substorm cycles and quasi-balanced reconnection. Note that the ECPC model is the general case as it can predict quasi-steady, quasi-balanced reconnection (if the interplanetary conditions driving dayside reconnection vary slowly enough) as well substorm cycles. On the other hand, balanced reconnection is not the general case as it cannot predict substorm cycles (nor is there any known mechanism that can act to balance the reconnection rates at any one instant). *Lockwood* (1991) pointed out that the motion of adiaroic convection reversals boundaries means that they are smoothed out in average patterns of convection. On timescales shorter than the substorm cycle of polar cap expansion and contraction, ionospheric convection reflects both the DP-2 and DP-1 current systems and displays the

response delays associated with both (respectively a few minutes and 30-60 min). In addition, because of a combination of ionospheric incompressibility and the antisunward motion of open field lines, the response delay varies with location, increasing with distance away from noon (*Lockwood et al.*, 1986; *Saunders et al.*, 1992; *Lopez et al.*, 1999; *Morley and Lockwood*, 2005).

Convection is often quantified by the transpolar voltage Φ_{PC} between convection reversal boundaries in the ionosphere on the dawnside and the duskside of the polar cap (*Reiff et al*., 1981; *Cowley*, 1984*; Boyle*, 1997; *Hairston et al*., 1998; *Liu et al*., 2019). This parameter is measured by spacecraft in high-inclination, Low-Earth Orbit (LEO) by integration of the observed "along-track" component of the electric field along the satellite path between the two dominant Convection Reversal Boundaries (CRBs). That electric field can be either directly measured or derived from observations of the vector magnetic field, $\vec{B}$ and the plasma flow $\vec{V}$ and using the equation of ideal MHD $\vec{E} = -\vec{V}\times\vec{B}$ which applies to a very high degree of accuracy even in the F-region ionosphere because of the high magnetic Reynold's number (*Hanson et al.*, 1994). Hence by integrating the along-track electric field (corresponding to the cross-track drift) between the two main CRBs, the transpolar voltage Φ_{PC} is measured for that satellite path. The quantity Φ_{PC} is often accurately called the "polar cap potential drop", but also frequently (but inaccurately) referred to as the "cross-cap potential" or "polar cap potential". Strictly speaking, it is a potential difference, i.e., a voltage, and this semantic point has real physical significance to understanding because, by Faraday's induction law, a voltage is synonymous with magnetic flux transfer rate whereas a potential is not. Hence, we here use the term "transpolar voltage" for Φ_{PC} and note that it is the rate at which magnetic flux is transferred across the polar cap. One convention that can be used is that positive transpolar voltage means that the dawnside CRB potential exceeds the duskside CRB potential (i.e., the electric field is from dawn to dusk), and this applies most of the time because net flux transfer is from the dayside to nightside. The reason for this is that open flux is, by definition, embedded in the solar wind flow and the solar wind is always transferring that open flux antisunward and, during even the longest intervals of northward IMF, the open flux never decays away. This antisunward flux transport remains dominant during northward IMF despite interruptions by intervals of sunward flow of some open flux tubes caused by them being reconfigured by lobe reconnection taking place at the magnetopause at the sunward edge of the tail lobes (see review by *Lockwood and Moen*, 1999). In terms of

magnetospheric configuration and voltages, this means the geomagnetic tail is always present and so magnetic shear is always present between the two tail lobes giving some level of magnetic reconnection in the associated cross-tail current sheet. In addition, reconnection at the low-latitude dayside magnetopause (i.e., between the magnetic cusps) that opens geomagnetic field lines has been observed to continue (at a low level) during intervals of northward IMF (*Chandler et al*., 1999; *Fuselier et al.*, 2000).

Figure 1 is a schematic of the three drivers of convection in the magnetosphere and ionosphere during southward IMF. This is adapted from *Cowley* (1982), but with the addition of a reconnection X-line in the cross-tail current sheet (in green, the voltage across which is Φ_N) that re-closes open field lines. This is included here because in the ECPC model (*Cowley and Lockwood*, 1992) it contributes to the ionospheric transpolar voltage Φ_{PC}. The ECPC model predicts that at any one time, the effect of Φ_N combines with the effect of the reconnection voltage Φ_D along the dayside magnetopause reconnection X-line (in red) which generates open field lines. The third source of Φ_{PC} illustrated here is "viscous-like" momentum transfer across the magnetopause onto closed field lines that generates a total antisunward magnetic flux transfer of closed flux of voltage Φ_V in the low latitude boundary layers (LLBL) on the dawn and dusk flanks of the magnetosphere. Figure 2 is a schematic of ionospheric flow patterns that is compatible with Figure 1 and the ECPC model in general. Figure 2a shows the special case of steady-state ($\Phi_D = \Phi_N$) with some viscous-like flow cells ($\Phi_V > 0$) and is as in the schematic used by *Cowley* (1982). Figures 2b and 2c are examples of ECPC model predictions for, respectively, an expanding and a contracting polar cap. For polar cap expansion $\Phi_D > \Phi_N$ and $\Phi_{PC} \approx \Phi_D$. For a contracting polar cap $\Phi_N > \Phi_D$ *and* $\Phi_{PC} \approx \Phi_N$. In Figures 2b and 2c, no viscous flow excitation is included ($\Phi_V = 0$), but several features often mistaken for viscous-like flows are seen in Figure 2c. In particular, the convection pattern shows flow streamlines entering the polar cap over the entire dayside and the transpolar voltage exceeds the dayside reconnection voltage ($\Phi_{PC} \approx \Phi_N > \Phi_D$).

The presence of lobe stirring cells during northward IMF, or even lobe field line re-closure by reconnection at the sunward edges of both lobes (e.g. *Lockwood and Moen*, 1999), means that northward IMF is inherently a non-steady-state situation because, by Faraday's law, the electric field has a curl with dawn-to-dusk electric field associated with reconnection in the cross-tail current sheet but dusk-to-dawn electric field along the lobe reconnection site(s) at

187 the sunward edge(s) of the lobe magnetopause (*Lockwood*, 2019). Hence during the 50% of
188 time that the IMF points northward (*Hapgood et al*., 1991; *Lockwood et al.*, 2017; 2019b) the
189 magnetosphere is quiet but also inherently in a non-steady state because of the slow decay of
190 open flux (see review by *Lockwood*, 2019).

191 Figure 3 gives two schematics of a northern hemisphere convection pattern that we would
192 expect during northward IMF; specifically, if the IMF has (a) components $B_Z > 0$ and $B_Y =$
193 0 and (b) $B_Z > 0$ and $B_Y > 0$ in the GSM reference frame. Figure 3(a) shows the case of
194 lobe reconnection (voltage Φ_L) driving symmetric lobe circulation cells in the open polar cap,
195 as well as the effects of reconnection voltages Φ_D and Φ_N and a viscous-like voltage Φ_V. In
196 Figure 3(b), the magnetic curvature force on newly-reconfigured open field lines for the large
197 positive IMF B_Y causes the dawn lobe cell to dominate: note in this case how the poleward
198 contraction of the (dusk) adiaroic open polar cap boundary causes the sunward flowing
199 portion at lower potentials of this one lobe convection cell to merge with the main dusk cell.

200 Because we here survey a very large dataset, we need to automate the scaling of transpolar
201 voltage and we found that automated algorithms to distinguish and identify lobe cells from the
202 cells driven by Φ_D , Φ_N and Φ_V were not reliable, particularly given that the merging of lobe
203 and main flow cells illustrated in Figure 3b is often seen for northward IMF conditions. To
204 enable automated scaling, we here define Φ_{PC} by

205 $$\Phi_{PC} = \phi_{max} - \phi_{min} \qquad (1).$$

206 We apply this, irrespective of the locations at which the maximum (ϕ_{max}) and minimum
207 (ϕ_{min}) of the potential pattern occurs . This is good for investigating the ECPC model because
208 it allows for the sunward and antisunward shifts of the locations of both ϕ_{max} and ϕ_{min}
209 caused by dominant Φ_D and Φ_N, respectively (see Figures 2b and 2c). The maximum
210 potential ϕ_{max} is usually the potential at the centre of the main convention cell on the dawn
211 flank of the polar cap (ϕ_{dawn1} in Figure 3) and the ϕ_{min} is usually the potential at the centre
212 of the main cell on the dusk flank of the polar cap (ϕ_{dusk1} in Figure 3). However, if the lobe
213 reconnection voltage Φ_L is large enough, ϕ_{max} can become ϕ_{dusk2} and/or ϕ_{min} can become
214 ϕ_{dawn2}, where ϕ_{dusk2} and ϕ_{dawn2} appear across the ends of the footprint of the lobe
215 reconnection X-line and are also defined in Figure 3. Hence if $\phi_{dusk2} > \phi_{dawn1}$ and

$\phi_{dawn2} < \phi_{dusk1}$, our definition means that $\Phi_{PC} = \phi_{dusk2} - \phi_{dawn2} = \Phi_L$. We will call Φ_{PC} in this case a "lobe-dominated" value of Φ_{PC}: note that it is a positive value even though the dominant flow in the central polar cap is now sunward. If neither lobe cell sets ϕ_{min} or ϕ_{max} then Φ_{PC} is the voltage associated with antisunward convection over the polar cap set by Φ_D , Φ_N and Φ_V. We note below that this is the most common situation and hence we call the resulting $\Phi_{PC} = \phi_{dawn1} - \phi_{dusk1}$ a "conventional" value. There is a third possibility where $\phi_{dusk2} > \phi_{dawn1}$ or $\phi_{dawn2} < \phi_{dusk1}$ but not both. In either of these two cases, Φ_{PC} will be somewhat larger than the conventional value and we call this a "hybrid" value as Φ_D, Φ_N, Φ_V, and Φ_L can all contribute to Φ_{PC}. *Wilder et al.* (2008) have surveyed SuperDARN data and shown that the lobe reconnection voltage in the ionosphere Φ_L saturates at about 15-20 kV. This means that voltages above 20kV are almost all "conventional" values associated with dominant antisunward transfer of flux over the polar cap and set by Φ_D , Φ_N and Φ_V. However for Φ_{PC} < 20kV we need to remain aware that Φ_D, Φ_N, Φ_V, and Φ_L can all contribute to Φ_{PC} for the hybrid cases and that for the lobe-dominated cases $\Phi_{PC} = \Phi_L$. For our definition, the viscous-like voltage Φ_V would only equal the Φ_{PC} value if all three reconnection voltages Φ_D, Φ_N and Φ_L were zero.

Milan et al. (2021) surveyed one-year of data and found that roughly 20% of all antisunward magnetospheric flux transfer was during quiet periods, 43% during non-steady-state phases (20.8% substorm growth, 9.8% substorm expansion, 3.3% substorm recovery, 1.2% recovery bays and 8% multiple intensifications). The remaining 37% was during intervals they classed as "driven" – these include extended substorm growth phases and periods when dayside and nightside reconnection are close to being balanced ($\Phi_D \approx \Phi_N$). This driven state was found for 18.2% of the time, compared to 27.2% of the time for the non-steady phases. Together these make up the 50% of time for which the IMF points southward and, as noted above, northward IMF is inherently non-steady and so non-steady conditions are present 77.2% of the time. Hence, in both time and resulting flux transfer, non-steady conditions are the dominant magnetospheric response. However, we introduce steady state into our view of the coupled magnetosphere-ionosphere system at all times if we average data together. In steady-state, the rate of flux transfer across the polar cap, Φ_{PC} equals the rate at which field lines are opened by reconnection in the dayside magnetopause (the dayside reconnection voltage Φ_D) and the rate at which open field lines are closed by reconnection in the cross-tail current sheet

(the nightside reconnection voltage Φ_N), plus any non-reconnection "viscous-like" voltage, Φ_V (i.e. $\Phi_{PC} = \Phi_D + \Phi_V = \Phi_N + \Phi_V$). The balanced reconnection ($\Phi_D \approx \Phi_N$) needed for steady state can occur at any one moment by chance or could be the result of a mechanism that maintains it. As yet, no such mechanism has been defined. Furthermore, there are reasons to believe that no such mechanism can be present: for it to operate, information about the magnetopause reconnection voltage at any one time Φ_D would have be able to reach the nightside reconnection site so the mechanism can modulate Φ_N. Because of propagation delays, at the nightside reconnection site there can be no information about the instantaneous value of Φ_D at the dayside reconnection site, and so $\Phi_D \approx \Phi_N$ cannot happen as a matter of course, maintained by a balancing mechanism. Faraday's law applied to the open-closed field line boundary gives the general behaviour:

$$dF_o/dt = B_i . dA_o/dt = \Phi_D - \Phi_N \qquad (2)$$

where F_o is the open magnetospheric flux, A_o the area of the open field line polar cap in the ionosphere and B_i is the magnitude of the field in the ionosphere (in this equation, B_i is assumed to be constant). Note that Equation (2) can be thought of as the continuity equation for the open flux F_o. Hence steady state requires $\Phi_D = \Phi_N$ and $dF_o/dt = dA_o/dt = 0$ and the fact that the polar cap area varies shows that non-steady conditions apply (*Holzer et al.*, 1986; *Milan et al., 2003; Milan*, 2004). The results of *Lockwood et al*. (2009) and *Milan et al*. (2021) show that non-steady state is a common situation, which is to be expected because of the variability in the IMF orientation (and hence Φ_D) and the fact that the transfer of information from the dayside magnetopause reconnection site to that in the cross-tail current sheet takes time and hence Φ_N can only respond after a lag. How common balanced convection ($\Phi_D \approx \Phi_N$) events are found to be is a matter of definition (see *McWilliams et al*., 2008) and they will be less common if tighter limits are placed on the maximum ($\Phi_D - \Phi_N$) used to define them. For a large averaging timescale τ, the time derivatives in equation (2) tend to zero because long-term trends in F_o and A_o are negligibly small. So, for large enough τ

$$< \Phi_{PC} >_\tau - < \Phi_V >_\tau = < \Phi_D >_\tau = < \Phi_N >_\tau \qquad (3)$$

even though this condition only applies relatively rarely at any one instant of time during southward IMF.

The voltage Φ_V is generated by any non-reconnection process transferring momentum from the flow of the shocked solar wind in the magnetosheath to closed field lines (e.g., *Farrugia et al*., 2001). The ECPC model predicts that Φ_V is small and that most of what had previously been thought to be voltage driven by viscous-like processes is, in fact, due to the nightside reconnection voltage Φ_N which always persists because the geomagnetic tail never erodes away and so there is always magnetic shear in the centre of the tail (*Wygant et al.*, 1983, *Lockwood et al.*, 1990; *Lockwood*, 1991; *Milan*, 2004). Numerical simulations have confirmed that Φ_N contributes to transpolar voltage Φ_{PC} in addition to Φ_D (e.g., *Gordeev et al.*, 2011).

Lockwood (1991) pointed out that a consequence of the ECPC pattern is that Φ_{PC} for a given Φ_D, Φ_N and Φ_V will depend on the shape of the open polar cap and how it is changing and only for an open polar cap that remains circular at all times is the voltage across the centre of the polar cap equal to $\Phi_V + (\Phi_D + \Phi_N)/2$. Hence, in general, for the duration of each polar cap traversal by a LEO satellite we need to consider non-steady conditions, and that each Φ_{PC} value observed will depend on Φ_D, Φ_N, and Φ_V and on how the polar cap is changing shape (i.e., the motion of the adiaroic boundaries which reflect the potential distribution along the boundary) and, critically, on the satellite path. Some changes in the polar cap shape are an integral part of the ECPC flow excitation mechanism proposed by *Cowley and Lockwood* (1992), specifically the equatorward expansion around noon caused by sudden increases in Φ_D and the poleward contraction around midnight caused by sudden increases in Φ_N. However, other polar cap shape distortions are likely. Examples include the effects of changes in the IMF B_Y component (*Lockwood, 1991; Cowley et al*., 1991b) or transient and propagating filamentary field aligned currents in Travelling Convection Vortices induced by solar wind dynamic pressure pulses (e.g., *Lühr et al.*, 1996). In addition, prolonged northward IMF can lead to open flux collecting towards midnight, giving a more triangular open flux region characteristic of the "horse-collar" pattern in global auroral images (*Hones et al.*, 1989; *Birn et al.*, 1991): it has been proposed that this is enhanced by lobe reconnection taking place in both hemispheres which removes dayside open flux (*Milan et al.*, 2020). Hence the use of a circular open polar cap in Figures 2 and 3 is illustrative only. Nevertheless, in general, passes of the dayside polar cap will reflect the influence of Φ_D to a greater extent and for passes over the nightside polar cap the influence of Φ_N will be greater.

The question then arises as to what is the minimum averaging timescale τ required to make equation (3) apply to a good approximation? Clearly, τ smaller than about 3 hours is inadequate as it is comparable to the timescales of the substorm cycle over which the open polar cap expands and contracts (*Holzer et al.*, 1986; *Lockwood et al.*, 1990; *Lockwood and Cowley*, 1992, *Milan et al*., 2003; 2009; 2012; *Huang et al.*, 2009). *Imber et al.* (2013) show that over the sunspot cycle the polar cap area is remarkably constant, making dF_o/dt negligible over timescales τ of order years. Both modelling (e.g., *Lopez et al.,* 2001) and observational studies (e.g., *Mishin and Karavaev,* 2017) show that F_o rises during the initial phases of large geomagnetic storms but F_o, like Φ_{PC} (e.g., *Kubota et al.*, 2017), appears to saturate establishing a temporary quasi-steady state, before falling again as the storm declines. These "Balanced Reconnection Intervals" (BRI) are related to the phenomenon of "Steady Magnetospheric Convection" (SMC) (*McWilliams et al*., 2008) events but do not necessarily start with a substorm growth phase nor end with a substorm expansion phase (*DeJong et al*., 2008); however, because in general there is a long-term variation in F_o around both BRI and SMC events (*Lockwood et al.*, 2009 ; *Milan et al.*, 2021) they cannot be considered a steady-state phenomenon on timescales shorter than their duration. However, we note that some BRI and SMC events probably can occur without prior, or subsequent, major change in F_o and these would be chance occurrences of matched Φ_N and Φ_D variations or because the rate of change in Φ_D has been slow enough for Φ_N to respond despite the propagation lag. Note also that the high variability of IMF orientation, and hence power input into the magnetosphere gives this a lower occurrence frequency than that non-steady conditions (*Lockwood et al*., 2019b; c).

In general, we need τ to exceed storm durations for steady state to fully apply. *Haines et al.* (2019) have surveyed geomagnetic storms in the homogeneous aa index, aa_H (*Lockwood et al.*, 2018a; b) since 1868, defining storms as when aa_H exceeded its overall 90th percentile: of the 10^4 storms defined by this threshold, none lasted more than 3 days. Hence $\tau \geq 3$ days should generally make steady-state a valid assumption. We note that *Weigel* (2007) proposes that the time constant is considerably longer than this, such that non-steady conditions and solar wind history even means that the time of year influences the variation; however, as demonstrated by *Lockwood et al.* (2016), this would generate an "axial-like" time-of-day/time-of-year pattern and we can discount this proposal.

1-ii. SuperDARN Transpolar Voltage Data and Potential Patterns

The studies of transpolar voltage discussed in the previous section were made using observations of electric fields and plasma flows by LEO satellites as they passed over the polar caps. One problem with this is that the satellite path will not generally intersect the points of maximum and minimum potential and so the difference between them, the full transpolar voltage Φ_{PC}, will be systematically underestimated. In addition, because there is no information of the potential pattern away from the satellite path, there is no way of checking if, or by how much, any one value is an underestimate. Studies have generally used passes that are close to the dawn-dusk meridian to try to minimise this problem, but the ECPC model predicts that this will only work for steady state conditions. This is because, as illustrated by Figures 2b and 2c, for dominant magnetopause reconnection ($\Phi_D > \Phi_N$), both the maximum and minimum of the potential pattern will be shifted towards noon and for dominant tail reconnection ($\Phi_N > \Phi_D$) they are shifted towards midnight. In this paper we use values derived from the SuperDARN (Super Dual Auroral Radar Network) coherent radar arrays (see review by *Chisham et al*., 2007). By imaging the convection pattern, the points of maximum and minimum potential can be identified and the problem inherent in the spacecraft data avoided. As discussed in Section 1-i, we adopt the definition $of\ \Phi_{PC}$ given in equation (1) and use an automated algorithm to compute it from patterns of the ionospheric potential, ϕ.

However, there are some other important points to note about the transpolar voltage data from the SuperDARN radars. The radars monitor the line-of-sight component of the flow of F-region plasma by measuring the Doppler shift of coherent echoes that have reflected off convecting ionospheric irregularities embedded in the bulk plasma flow. The most accurate method for generating two-dimensional field-perpendicular convection velocity vectors from the SuperDARN radar data is by combining the line-of-sight measurements within a common field-of-view of pairs of radars (e.g., *Greenwald et al.*, 1995). However, because of the aspect sensitivity of echoes with respect to the structures causing the scatter, for much of the time when echoes are recorded by one radar, they are not detected by the twin radar looking in a different direction and so opportunities to make these "bistatic" observations are relatively rare. Hence methods to find the functional form for the distribution of electrostatic potential ϕ that was a best fit to all the line-of-sight velocity measurements were developed (*Ruohoniemi*

and Baker, 1998; *Cousins et al.*, 2013). The most widely used of these is the "map-potential" technique (a form of re-analysis using data-assimilation), which performed well when tested against available bistatic vectors (*Provan et al.*, 2002). However, lack of radar coverage and/or of the required scattering irregularities mean that line-of-sight data are not available at all locations in the polar regions and so the velocity data are supplemented with predictions by a statistical model, driven by the IMF conditions observed by an upstream monitor. From each derived map-potential pattern the transpolar voltage Φ_{PC} can be scaled (*Bristow et al*., 2004; *Wilder et al.*, 2011). A review of the development and application of this technique has been presented by *Chisham et al.* (2007).

The statistical model predictions used in the map-potential technique are weighted to minimize their impact for a given number of available radar echoes, n_e (*Shepherd and Ruohoniemi*, 2000). At times there are sufficient numbers and wide enough spatial distribution of echoes for the potential pattern to be determined from the radar data alone; on the other hand, in extreme cases with no echoes ($n_e = 0$), the pattern is determined purely by the model and hence by the observed upstream interplanetary conditions. Tests of flow velocities derived using the SuperDARN radars have been made by comparing the map-potential flow estimates with data from the Defense Meteorological Satellite Program, DMSP (e.g., *Xu et al.*, 2007a; b; *Drayton et al*., 2005) and Swarm (*Koustov et al.*, 2019a) spacecraft. In addition, transpolar voltage data from the SuperDARN map-potential data have been compared to those derived by the AMIE (Assimilative Mapping of Ionospheric Electrodynamics) technique that uses a variety of sources, particularly magnetometers (*Gao*, 2012). Given that there is a tendency for flow speeds defined by SuperDARN to be about 30% lower than seen by satellites (*Xu et al*., 2007b; *Drayton et al.*, 2005; *Koustov et al*., 2019a), but that convection reversal boundary locations in the two data sets are very similar, we would expect SuperDARN values of Φ_{PC} to be well correlated with the satellite values but typically 30% lower. From the detailed comparison shown in part (c) of Figure A1 in Appendix A, allowing for the effect of the number of data echoes n_e and the proximity of the satellite pass, we find a similar result but the best fit regressions (linear and non-linear) show that the radar values are typically 20% lower.

In this paper we use a variety of threshold values n_{min} of the number of radar echoes n_e to investigate the effect of low n_e on our results. All Φ_{PC} values based on $n_e < n_{min}$ echoes

were discarded, and we varied n_{min} to determine the sensitivity of our results to the choice of n_{min}.

The use of a $n_e > n_{min}$ selection criterion has an important but subtle implication for biases in the data because considerably fewer echoes are received during summer. This is probably due to combination of causes acting together including: sporadic E-blanketing of F-region radar returns; interference from enhanced ground echoes; a smoother ionosphere when photoionization rate is high and the effects of radar transmitter frequency selection (*Koustov et al.*, 2019b and references therein). Here, we only use potential maps from the northern hemisphere radar array with its greater number of stations and the means of n_e are consistently about 200 around the June solstice (summer) whereas they are typically between 500 and 600 around the December (solstice) winter. This means that hourly values that meet, for example, a $n_e > n_{min} = 255$ criterion are quite rare in summer and atypical (around 2-3 per day, whereas there are typically 20-24 per day in winter).

The other factor that we need to be aware of is that the occurrence of echoes also increases with the plasma velocity (*Koustov et al.*, 2019b). This means that although we want to avoid samples with low n_e to minimise the role that the data-assimilation statistical convection model plays in the Φ_{PC} value, we do not want to eliminate too many samples because that would preferentially remove low-flow (and hence low-Φ_{PC}) samples.

The ECPC model has been used quantitatively to match to map-potential SuperDARN observations of the evolution of the convection pattern and Φ_{PC} following individual events of southward and northward turnings of the IMF (*Lockwood et al.*, 2006), events that were also quantitatively compared with the associated signatures of magnetopause reconnection in cusp proton precipitation and aurora (*Lockwood et al.*, 2003; *Throp et al.*, 2005). Here we make a statistical study of the Φ_{PC} data from SuperDARN using data from 25 years – more than a full Hale solar magnetic cycle.

2. Data Employed

In this paper we make use of 214410 hourly observations of the ionospheric transpolar voltage Φ_{PC}, as defined by equation (1), derived from map-potential ϕ patterns obtained by the northern-hemisphere SuperDARN radar network between 1995 and 2020. These data are

generated by applying the map-potential technique to data from 2-minute integration periods and the 30 values of Φ_{PC} and n_e in each hour were then averaged together. The processed data have been checked using comparisons with dawn dusk passes by DMSP satellites from 2001-2002 for which the SuperDARN convection patterns show potential minima and maxima close to the satellite path (see Appendix A).

We compare with data on the north-south component of the IMF in the GSM frame, B_Z (defined positive northward), and the solar wind dynamic pressure, p_{SW}, both taken from the OMNI dataset, compiled and maintained by NASA's Goddard Space Flight Center (*King and Papitashvili*, 2005). We also compare with the AL auroral electrojet geomagnetic index compiled and maintained by the World Data Centre for Geomagnetism, Kyoto. We use one-minute values of B_Z, p_{SW} and AL. Because we are not sure of the precise propagation lags of these parameters relative to the Φ_{PC} data we take running (boxcar) means over a timescale τ which we then interpolate to the mid-point of the hour over which Φ_{PC} data are averaged, minus a nominal lag δt. We repeated all studies using two values of τ, $\tau = 1\ hr$ to match the averaging timescale of the Φ_{PC} data and $\tau = 15\ min.$: plots for the two were almost identical and we use $\tau = 15\ min.$ in the plots shown. For IMF B_Z we use a lag $\delta t = 5\ min.$, to allow for propagation across the magnetosheath to the dayside magnetopause reconnection X-line and then down geomagnetic field lines to the ionosphere, because we are interested in the effect of IMF B_Z on the dayside reconnection voltage Φ_D. For p_{SW} we have tried two different values of δt: to search for an effect of p_{SW} on Φ_D we use $\delta t = 5\ min$ as for IMF B_Z, and to search for an effect of p_{SW} on Φ_N we use $\delta t = 75\ min$ (derived below). The latter effect is expected from squeezing of the near-Earth tail, as recently observed and modelled by *Lockwood et al.* (2020a; b; 2021). Because of the persistence (i.e., a high and broad autocorrelation function) in the p_{SW} data series, the results are similar for the two δt values; however, slightly clearer effects are seen for $\delta t = 75$ min. and that is the value employed in the plots presented here. For AL, we use $\delta t = 0$ as both AL and the Φ_N value are used as an indicator of signatures in the nightside auroral ionosphere. We compute $p_{SW} = m_{SW} N_{SW} V_{SW}^2$ from 1-minute values of the solar wind mean ion mass m_{SW}, number density N_{SW} and speed V_{SW}; in the case of m_{SW} these are linearly interpolated from 5 min., 15 min or hourly observations if 1-min. values are unavailable.

We note that a great many papers derive propagation delays δt between solar wind features and responses in the magnetosphere and ionosphere. These are not always comparable because different solar wind features and different responses are considered. In addition, some effects call for IMF orientation to be considered whereas others do not. In addition, the solar wind speed varies and alters the δt values. Some studies use correlations to define the peak response whereas other use the timing of the first detectable response. A detailed and extensive statistical study of the delay between changes in the IMF B_Y component and their effect appearing in the near-Earth tail lobes and plasma sheet was presented by *Browett et al.* (2017). They found optimum delays of 1 hr for southward IMF but up to 5 hr for northward IMF conditions. Because these are the times for the magnetic curvature force to take effect in the tail, they relate to field-aligned Alfvén wave propagation times as well as solar wind propagation times and so are not directly comparable with, for example, the propagation time for dynamic pressure change effects in the tail. We note that the value of $\delta t = 75\ min$ that we here derive and use, is slightly longer than the $60\ min$ that *Browett et al.* (2017) derive for southward IMF but much shorter than 300 min that they find sometimes derived for northward IMF.

3. Results

3-i. Effect of number of radar echoes, n_e

Figure 4 shows the cumulative probability distribution (c.d.f.) of the number of radar echoes n_e for the 214410 samples of the ionospheric transpolar voltage, Φ_{PC}. The vertical coloured lines show a set of nominal values of n_{min}, which we vary from 100 (dark red) to 900 (mauve) in steps of 100 in our sensitivity study (i.e., n_{min} = [100:100:900]). These values yield subsets of 137633, 85078, 52501, 32646, 20378, 12866, 8032, 4958, and 3134 samples. The black dashed line is for n_{min} = 255 which we discuss below, and which yields 60653 samples, very close to 30% of the original dataset.

Figure 5 shows the probability distribution functions for hourly transpolar voltage, Φ_{PC}, selected using the condition $n_e > n_{min}$ for the values of n_{min} used in Figure 4. It can be seen that the shape of the distribution varies with n_{min}, the mode value of the normalised distribution getting smaller and moving to higher values. The large-value tail of the

488 distribution therefore gets relatively larger, as expected from the discussion in section 1-ii. It
489 can be seen that for n_{min} < 300 the effect on the distribution shape is, however, relatively
490 minor.

491 To further define an optimum value for n_{min} we have carried out a comparison with dawn-
492 dusk passes by DMSP satellites for the years 2001 and 2002 and compared the transpolar
493 voltage derived, $[\Phi_{PC}]_{\mathrm{DMSP}}$, with the simultaneous SuperDARN map-potential estimates,
494 $[\Phi_{PC}]_{\mathrm{S.DARN}}$. We computed the root mean square deviation, $(< \Delta\Phi_{PC}^2 >)^{1/2}$ (where $\Delta\Phi_{PC} =$
495 $[\Phi_{PC}]_{\mathrm{DMSP}} - [\Phi_{PC}]_{\mathrm{S.DARN}}$) as a metric of agreement. In general, we found $\Delta\Phi_{PC}$ tended to
496 be positive, consistent with the studies discussed in section 1-ii. We used the Nelder-Mead
497 search to find a minimum in $(< \Delta\Phi_{PC}^2 >)^{1/2}$ as a function of n_{min} and the maximum allowed
498 geocentric angular separation of the satellite and radar potential maxima and minima, δ. This
499 yielded an optimum n_{min} of 255 and for the optimum maximum δ of 30° . The use of n_{min} =
500 255 gave a peak correlation between $[\Phi_{PC}]_{\mathrm{DMSP}}$ and $[\Phi_{PC}]_{\mathrm{S.DARN}}$ of 0.85 with and r.m.s.
501 deviation $(< \Delta\Phi_{PC}^2 >)^{1/2} = 18.5\ kV$, compared to a correlation of 0.82 for $n_{min} = 0$, for
502 which $(< \Delta\Phi_{PC}^2 >)^{1/2} = 21.2\ kV$ (see Appendix A). Hence agreement was most improved
503 by adopting of n_{min} = 255 which is a value small enough not to greatly change the shape of
504 the overall distribution of $[\Phi_{PC}]_{\mathrm{S.DARN}}$ values, as shown by Figure 5. We also used this
505 survey to calibrate the SuperDARN estimates: where comparisons are made, we here correct
506 the systematically higher values (by a factor of 20%) from the satellite observations using the
507 linear regression of the $[\Phi_{PC}]_{\mathrm{DMSP}}$ and $[\Phi_{PC}]_{\mathrm{S.DARN}}$ data for n_{min} = 255 and $\delta <$ 30° (see
508 Appendix A).

509 In sections 3-ii to 3-iv of this paper we employ the selection criterion $n_e > n_{min}$ = 255
510 (which gives us 60653 samples). However, in section 3-v we return to using all the n_{min}
511 values used in Figures 4 and 5 in a sensitivity study to show that our conclusions are not
512 influenced by the value of n_{min} adopted.

513 **3-ii. Variation of Φ_{PC} with IMF B_Z and the *AL* index**

514 Figure 6 analyses the optimum propagation lags needed for this study. The black line is the
515 lag correlogram (linear correlation coefficient as a function of lag) for Φ_{PC} and the IMF $-B_Z$
516 value (in the GSM frame). The peak correlation is with Φ_{PC} lagging behind B_Z by δt = 20

517 min. This is longer than the response time for dayside magnetopause reconnection (*Etemadi*
518 *et al.*, 1988; *Todd et al.*, 1988): from the propagation delay to cross the magnetosheath, this is
519 expected to be about 5 min. which is the typical response time seen in the observational
520 studies discussed in section 1-i. The propagation of the enhancement to the centre of the
521 polar cap was modelled using the ECPC model by *Morley and Lockwood* (2005) and a value
522 of 20 minutes from the nose of the bow shock is broadly consistent with their predictions.
523 Figure 2b shows that if the nightside reconnection voltage Φ_N is small, the transpolar voltage
524 Φ_{PC} is approximately equal to Φ_D and if we also fold in a non-zero viscous voltage this
525 becomes $\Phi_{PC} \approx \Phi_D + \Phi_V$. In addition, Figure 2b shows that this voltage appears between
526 maximum and minimum potentials at points that are close to the ends of the ionospheric
527 footprint of the magnetopause reconnection X-line. In this case the response of Φ_{PC} to IMF
528 B_z would be after the short lag with which Φ_D responds (i.e., $\delta t \approx 5\ min$). The AL index is
529 expected to be a good proxy for the nightside voltage Φ_N, becoming more negative as Φ_N
530 increases. Hence a subset of the data selected for a small $-AL$ should be give Φ_{PC} values
531 dominated by Φ_D and hence showing a small response lag. For the subset of data when the AL
532 index is above 100 nT ($i.e., -AL < 100nT$), shown by the blue line in Figure 6, the observed
533 lag of Φ_{PC} lag after B_z of $\delta t = 5\ min$ is therefore consistent with the ECPC model and low
534 Φ_N. A notable feature of all the correlograms in Figure 6, except those for Φ_{PC} and B_z (in
535 blue and black), is that the peaks are asymmetric with higher correlations at a given time after
536 the peak than for the same time before it. This shows that higher auroral activity (i.e., larger
537 negative AL) are responses over longer time constants and that time constant is variable.
538 The orange line shows that the optimum lag for the AL index after B_z is $\delta t = 35\ min$, but the
539 peak is lower and broader indicating there is considerable variability in that lag. The green
540 line gives the lag of the AL index after Φ_{PC} of $\delta t = 25\ min$, which yields a total lag of 25+20
541 = 45 min after IMF B_z which is 10 min longer than the value obtained from the direct
542 correlation between AL and IMF B_z. The mauve line shows the correlation between Φ_{PC} and
543 solar wind dynamic pressure p_{SW} which is considerably weaker than the other correlations, as
544 expected because Φ_{PC} depends primarily on Φ_D and Φ_N which are not expected to be as
545 strongly modulated by p_{SW} as they are by B_z. However, this Φ_{PC} versus p_{SW} correlogram
546 does show a broad, weak peak with a maximum at a lag of $\delta t = 120\ min$. This suggests that
547 if p_{SW} is exerting an influence on Φ_{PC} it is mainly via a modulation of Φ_N through squeezing
548 the near-Earth cross-trail current sheet. This will be discussed further in section 3-iii. The

correlation between Φ_{PC} and p_{SW} was also examined for northward and southward IMF conditions separately by selecting data when the B_z data simultaneous with p_{SW} was positive and negative, giving the cyan and grey correlograms, respectively. For southward IMF, the peak effect is soon after that of the peak response to IMF B_z and so this appears to show an influence of p_{SW} on the dayside reconnection voltage Φ_D. On the other hand, the peak response for northward IMF is at a lag of $\delta t = 75\ min.$ and because of the absence of large Φ_D in these cases, this appears to show a response of Φ_N to increased p_{SW} in these cases (see discussion by *Lockwood*, 2013). In our studies we used δt of 5, 75 and 120 min. for the optimum lag between p_{SW} and terrestrial responses: because of the high persistence in the p_{SW} data series the results were very similar in the three cases, and we here show values for $\delta t = 75 min.$

A great many studies have presented scatter plots of Φ_{PC} as a function IMF B_Z (or dawn-dusk interplanetary electric field $V_{SW}B_Z$, but the radial solar wind speed V_{SW} explains very little of the scatter) and shown that Φ_{PC} increases approximately linearly with $-B_Z$ for $B_Z < 0$ but has approximately constant and small values for $B_Z > 0$. Figure 7a shows that the SuperDARN dataset used here also confirms this behaviour by comparing a scatter plot of the Φ_{PC} values as a function of IMF B_Z (black points) with the corresponding scatter plot from the survey by of *Cowley* (1984) using data from a variety of LEO spacecraft (mauve points). Note that the satellite Φ_{PC} values have been reduced by the 20% factor found from comparisons with two years' passes by the DMSP satellites (see Appendix A). Because there are so many samples in our study, a scatter plot loses a great deal of information because so many points are plotted on top of each other. Hence in Figure 7b we color-code the fraction of samples ($n/\Sigma n$, on a logarithmic scale) in bins of narrow width in both Φ_{PC} and B_Z. The bins used are $\Delta B_z = 0.5nT$ wide in IMF B_z and $\Delta\Phi_{PC} = 2\ kV$ wide in the Φ_{PC}. The plot shows the features that are familiar from other plots. Two important features to note are that: (1) for southward IMF there is a considerable spread in Φ_{PC} at a given B_z; and (2) for northward IMF that spread decreases with increasingly positive B_z. The plot also shows that Φ_{PC} values increase slightly with increasingly positive B_z which implies that the lobe reconnection voltage Φ_L increasingly becomes a factor, as discussed in relation to Figure 3.

In the ECPC model, the spread at a given IMF B_z is expected because in non-steady state both Φ_D and Φ_N contribute to Φ_{PC}. From long-term averages (for which $\Phi_{PC} = \Phi_D + \Phi_V$)

we know that ($\Phi_D + \Phi_V$) varies approximately linearly with $-B_z$ for $B_z < 0$. It is also known that the auroral electrojet indices AE and AL vary approximately linearly with Φ_{PC}, again with considerable scatter (*Weimer et al*., 1990). In this paper we investigate the nightside auroral electrojet index AL as a proxy for the nightside voltage, Φ_N, which is consistent with its use as a substorm expansion phase identifier in substorm cycles. *Lockwood et al.* (2009) used satellite passes to show that, statistically, polar cap flux decayed (i.e., Φ_N is enhanced) during substorm expansion phases when $-AL$ is enhanced. *Hubert et al.* (2006) and *Milan et al*. (2009) used auroral images to also infer the loss of open flux during substorm expansion phases which also implies a relationship between $-AL$ and Φ_N. The variation of Φ_N inferred from time-constants by *Laundal* (2020) shows a strong variation with $-AL$, as does the analysis of the polar cap boundary location by *Aikio et al.* (2013).

Figure 7c shows the mean AL values in the same bins as used in Figure 7b and Figure 7d shows contours of these mean AL data. Note that these contours can only be fitted in areas where the data are not sparse (identified by Figure 7b). It can be seen that the spread in Φ_{PC} at a constant B_z is indeed associated with the spread in AL , as predicted by the ECPC model.

Figure 8a plots the variation of the occurrence of combinations of the AL index and IMF B_z using the same bins in B_z as used in Figure 7b and 7c and bins of AL that are 10 nT wide. Figure 8b shows the mean Φ_{PC} in the same bins as used in Figure 8a and Figure 8c shows the fitted contours of mean Φ_{PC} from the same data. The tilt of the contours towards the diagonal in 8b and 8c shows clearly that Φ_{PC} depends on both B_z and AL: at constant AL, Φ_{PC} increases with increasingly negative B_z (moving horizontally to the left of the plot) but importantly, Φ_{PC} also increases with increasingly negative AL at constant B_z for $B_z < 0$ (moving vertically up the left-hand half of the plot). Hence Φ_{PC} increases with increases in both IMF $-B_z$ and $-AL$.

3-iii. Evolution of Φ_{PC} during northward IMF with time since the IMF turned northward

A second scatter plot that was important verification of the ECPC model was presented in Figure 6 of *Wygant et al.* (1983). The plot looked at Φ_{PC}values during northward IMF, as a function of time Δt since the IMF last had a southward component. Shortly after a northward turning (small Δt), *Wygant et al.* found that almost the same range in Φ_{PC} was present as had

been seen during the prior periods of southward IMF. However, with increased time after the northward turning (larger Δt) this range decreased because the largest observed Φ_{PC} declined exponentially. This decline continued until after about 10 hours only low values of Φ_{PC} were seen. This behaviour is uniquely explained by the ECPC model which predicts that the larger values of Φ_{PC} seen when the IMF is northward are because there is a large Φ_N (despite Φ_D being small because the IMF was northward). Large Φ_N can still be present because of the large open flux that had been produced in the growth phase prior to the northward turning of the IMF, there being a delay before that flux is fully appended to the near-tail tail lobes by the solar wind flow. The inference was that the longer the IMF remained northward, the more events of higher Φ_N had depleted the open flux and so the maximum of subsequent events was reduced.

The *Wygant et al*. plot contained only 28 datapoints, it is here reproduced in Figure 9a for the 29373 datapoints available from our survey for IMF $B_z > 0$ and $n_e > 255$. To evaluate the time since the IMF had a southward component, we here use 6-minute boxcar running means of IMF B_z to avoid periods of northward IMF being interrupted by just a brief interval of southward IMF. For each northward-IMF Φ_{PC} value observed at time t_o we evaluate the time at which the IMF turned northward in these 6-minute running means, t_n, and hence $\Delta t = t_o - t_n$. We did also try using running means over 15 minutes and 60 minutes and Figure 9 was not substantially changed other than the appropriate resolution in Δt was lowered. Again, because of the large number of samples, we colour code the fraction of samples $n/\Sigma n$ (on a logarithmic scale) and all panels of Figure 9 uses bins in Φ_{PC} that are 2 kV wide (as in Figures 7 and 8) and in Δt that are 6 min wide. The near-exponential decay of the largest Φ_{PC} found by *Wygant et al*. is clear in Figure 9a and the time constant for that decay is very similar, with Φ_{PC} reduced to almost constant value by $\Delta t = 15\ hrs$. The ECPC model predicts that the larger Φ_{PC} values at a given Δt will be due to larger Φ_N and hence greater $-AL$. Figure 9b confirms that this is indeed the case by color-coding the mean of $-AL$ in the same bins as used in Figure 9a. *Wilder et al.* (2008) have used SuperDARN data to show that the lobe reconnection voltage in the ionosphere saturates at about 15-20 kV. From this we deduce that the voltages shown in Figures 9 for Δt greater than about 15 hours after the IMF turned northward are consistent with the effects of lobe reconnection. On the other hand, the values above 20 kV at Δt below about 10 hours (when AL is also enhanced) are not and we attribute these to enhanced Φ_N.

Because we are belatedly reproducing the highly significant plot by *Wygant et al*. (1983), it is worth making a direct comparison. This is done as two superposed scatter plots of Φ_{PC} as a function of time since the IMF was last southward Δt in the top panel of Figure 10. The black dots are from the present survey, the mauve dots the data of *Wygant et al.* (1983). As in Figure 7, the satellite Φ_{PC} values have been reduced by the 20% found in the comparison in Figure A1c of Appendix A. It can be seen that the trend inferred by *Wygant et al.* from their small data set is confirmed in our large survey. The lower panel shows the contours of mean $-AL$ in our survey and confirms the role of nightside reconnection invoked by the ECPC model explanation of the *Wygant et al.* plot.

3-iv. Effect of solar wind dynamic pressure, p_{SW}

In this section we investigate the effect of solar wind dynamic pressure p_{SW} on the tail of the magnetosphere. From Figure 6, we use p_{SW} values taken $\delta t = 75\ min$ before the corresponding AL and Φ_{PC} observation to allow for a propagation lag δt through the magnetosheath from the nose of the magnetosphere to sufficient distances down the tail to squeeze the tail reconnection site and so modulate the tail reconnection voltage Φ_N . The analysis was also carried out for $\delta t = 5\ min$ appropriate for the propagation from the nose of the magnetosphere to the dayside magnetopause and $\delta t = 120\ min$ that gives the peak correlation between p_{SW} and Φ_{PC}. The autocorrelation function of p_{SW} only falls to 0.5 at a lag of 6 hours and because of this great persistence in the p_{SW} data series, essentially the same features as shown here were observed for all three δt values used.

Figure 11 looks at the dependence on IMF B_z and the solar wind dynamic pressure (normalised by the mean, i.e., $p_{SW}/< p_{SW} >$) of (top) the mid-latitude am geomagnetic range index, (middle) the mean $-AL$ and (bottom) the mean transpolar voltage Φ_{PC}. In the left-hand panels averages are given in bins that are $\Delta B_z = 0.5\ nT$ wide in IMF B_z and 0.1 wide in $p_{SW}/< p_{SW} >$. The right-hand panels show fitted contours to these data and highlight the gradients (but unlike the mean values contours cannot be plotted in areas where the data are sparse). For all panels, values increase as we move to the left, i.e., with increasingly southward IMF. This is seen at all $p_{SW}/< p_{SW} >$ values. All parameters show an increase with $p_{SW}/< p_{SW} >$, at a given IMF B_z for $B_z > 0$ and for all three parameters this increase decreases as the IMF becomes increasingly southward (i.e., the tilted contours become progressively more vertical). For the am index we see clear increases with increasing p_{SW} at

all IMF B_z, although they are weaker for more strongly southward IMF. This effect of p_{SW} on am has recently been identified and modelled by *Lockwood et al.* (2020a; b; 2021) as being the effect of p_{SW} in squeezing the near-Earth tail. For both $-AL$ and Φ_{PC}, on the other hand the contours become vertical for strongly southward IMF and the effect of enhanced p_{SW} is no longer present. We infer AL and Φ_{PC} respond to increased Φ_N caused by the squeezing effect of p_{SW} on the magnetic shear across near-Earth cross tail current sheet, for northward IMF and for weakly southward IMF. From the studies of *Lockwood et al.* (2020a; b; 2021) we believe am also responds to the enhanced energy density stored in the tail lobes because of the same squeezing effect of p_{SW}. Figure 12 confirms the trends to higher values at higher p_{SW} by showing the mean values, averaged over all IMF B_z, with error bars of plus and minus one standard deviation: these are large because of the large variation introduced by B_z. The upward trend is seen in all three parameters but noticeably the gradient of the third-order polynomial fit decreases at larger p_{SW} for both AL and Φ_{PC}. The grey areas in Figure 12 are bounded by plus and minus 1-sigma error in the polynomial fit.

Figure 9c shows that the p_{SW} effect does play a role in the behavour during northward IMF. This plot is the same as 9a and 9b but shows the mean values of p_{SW} in the bins. It can be seen that the larger values of Φ_{PC} at a given time since the IMF turned northward tend to be at larger p_{SW}.

3-v. A sensitivity study of the effects of the availability of radar echoes

In the above sub-sections, all the plots shown are for the number of radar echoes $n_e > n_{min} = 255$. We have also generated all the plots using all of the 9 n_{min} $values$ given by the coloured lines in Figure 4. The trends in all plots are the same, the main effect being to change the absolute values in the means of Φ_{PC}. Figure 13 compares the variations of Φ_{PC} with IMF B_Z for the thresholds n_{min} of [100:100:900] (i.e., between 100 and 900 in steps of 100), shown in Figure 13b with that for $n_{min} = 255$ shown in Figure 13a. In Figure 13a the mean values and standard deviations are given for each B_Z bin as well as the 6th-order polynomial fit (solid line). In Figure 13b only the polynomial fits are plotted to avoid overplotting the multiple cases. It can be seen that the same behaviour is seen at all n_{min} values, the main difference being that Φ_{PC}values are systematically higher for larger n_{min} at all values of IMF B_Z. This is expected because removal of values based on low numbers of

echoes systematically removes low Φ_{PC} samples, as shown by Figure 5. We note that this effect is seen for both northward and southward IMF samples, except for the very largest (positive) B_Z when the mean Φ_{PC} is close to 25 kV, irrespective of the n_{min} used.

Figure 14 makes the equivalent comparisons of the average variations of Φ_{PC} for $B_Z > 0$ with time elapsed Δt since the IMF turned northward. Again the clear trend is to larger Φ_{PC} at larger n_{min}. However, this is not true at all Δt as the effect declines in amplitude at $\Delta t > 5hrs$ and is not seen at all at $\Delta t > 10hrs$, such that at the largest positive B_Z all n_{min} thresholds give a near constant Φ_{PC} of 15 kV.

We emphasise that all the plots presented in the Sections 3-ii, 3-iii and 3-iv have been generated using all 9 n_{min} thresholds of n_e used in Figures 4, 5, 13 and 14. In every case the form of the plot is essentially the same, the main effect being that there are fewer samples available and so the plots cover smaller ranges of the parameters as noise due to lack of samples becomes a greater issue in the tails of the distributions.

4. Discussion and conclusions

4-i. The dependence of transpolar voltage on magnetic reconnection in both the magnetopause and the cross-tail current sheet

We have regenerated two scatter plots that formed an important basis for the space physics community's understanding of magnetospheric and ionospheric convection. The plots of transpolar voltage as a function of the IMF B_z (for example, by *Reiff et al*., 1981; *Cowley*, 1984*; Boyle*, 1997; *Hairston et al*., 1998) were generated using typically less than 100 satellite passes. The plot by *Wygant et al.* (1983) of transpolar voltage as a function of time since the IMF was last southward was generated from just 28 data points. We here increase those numbers of data points by factors of over 1000 using convection patterns derived from the SuperDARN array of ground-based coherent radars.

We have used the AL auroral electrojet index to show that the scatter in these plots is well explained by the effect of the nightside voltage caused by reconnection in the cross-tail current sheet, as predicted by the Expanding-Contracting Polar Cap (ECPC) model (*Cowley and Lockwood*, 1992), and as was postulated in discussion and application of the model (e.g.,

Lockwood and Cowley, 1992; *Milan*, 2004; *Lockwood and Morley*, 2004; *Lockwood et al.*, 2006; *Milan et al.*, 2003; 2021). This has not been illustrated as clearly before now.

4-ii. Estimates of voltage due to viscous-like interaction across the magnetopause

We have demonstrated that the residual transpolar voltage after a period of southward IMF decays away with time elapsed since the IMF has been northward. After about 24 hours the voltage has decayed to $\Phi_{PC} \approx 15\ kV$ and although in general Φ_{PC} values are slightly sensitive to our choice of how many echoes are required (n_{min}) to yield a valid Φ_{PC} estimate, we have shown that this is not true for this estimate of the residual Φ_{PC} after long (~1 day) intervals of northward IMF. There are some points that should be noted about this value. From the above discussion, if both Φ_N or Φ_D could be considered to be zero at these times then we get a maximum estimate of the viscously-like voltage $\Phi_V < \Phi_{PC} \approx 15\ kV$.

Viscously-driven flows, by definition, appear in the region of closed field lines on the flank of the magnetosphere called the low-latitude boundary layer (LLBL, see Figure 1). One problem is defining what are closed field lines and *Fuselier et al.* (1999) have pointed out that some of the particle flux signatures traditionally used to identify closed field lines are actually best explained as open field lines. *Mozer* (1984) surveyed 24 LLBL crossings and found the voltage across the LLBL on one flank ranged between 0 and 16 kV, with an average of 3 kV. *Mozer et al.* (1994) surveyed 41 such crossings and found an average value of 4 kV. If such a voltage existed on both flanks simultaneously this implies a viscous voltage Φ_V in the range 0-32 kV with a mean value of 6-8 kV. These values are obtained by integrating the along-track electric field seen by magnetospheric spacecraft as they pass through the LLBL. *Hapgood and Lockwood* (1993) pointed out that an assumption in these measurements is that the LLBL is stationary and that the satellite moves through it so that the LLBL thickness is the speed of the satellite times the time it resides in the LLBL. However, in general a better approximation would be that the satellite be considered stationary and the boundary moves over it and that large estimates in LLBL thickness and Φ_V can arise from a boundary that happens to be moving with the craft. They used plasma characteristics in the LLBL to show that for some cases of apparently large viscously-driven voltage the true value was, in fact, only about 3 kV on one flank: if the same applied on the other flank Φ_V would be 6 kV. In theory, we should be able to use multi-spacecraft missions the pass through the LLBL to resolve boundary motions and compute LLBL thickness and voltage. Such missions include

AMPTE (Active Magnetospheric Particle Tracer Explorer), Cluster, MMS (Magnetospheric Multiscale Mission) and THEMIS (Time History of Events and Macroscale Interactions during Substorms). Although we can find several examples of the use of these spacecraft to determine LLBL thickness, a literature search has not revealed any further estimates of LLBL voltage. However, we note that *Lockwood and Hapgood* (1997) did use the AMPTE-IRM and AMPTE-UKS pair to show that the analysis of *Hapgood and Lockwood* (1993) was correct.

Detailed study of convection reversals in the ionosphere near dawn and dusk indicates that sometimes the plasma motion across them exceeds the motion of the boundary, implying they are not just moving adiaroic boundaries and there is a genuinely viscous-like process at work (*Lockwood et al*, 1988; *Chen and Heelis*, 2018); however, in such cases the true boundary motion is very difficult to determine accurately and uncertainties are large making accurate determination of Φ_V by integrating along the boundary almost impossible. *Newell et al.* (1991) and *Sundberg et al.* (2008) used LEO observations of electric fields and particle precipitations to infer the voltage across the low-altitude footprint of the LLBL and find values mainly below 10 kV with a few values over 20 kV. There are two problems with this which may explain the larger estimates of Φ_V. Firstly, the identification of closed LLBL field lines from the particle precipitations is not definitive. Secondly, the ECPC model predicts that antisunward flow on closed field lines in the ionospheric projection of the LLBL can be generated by nightside reconnection and polar cap contraction because the convection reversal boundary can be shifted from the open-closed field line boundary by the conductivity distribution in the ionosphere.

From the above, a mean value of Φ_V of around $8\ kV$ is appropriate and so the estimate of $\Phi_V \leq 15\ kV$ derived here from Figure 14, is somewhat higher than we would expect for an average value of past estimates. However, we stress here that this is a maximum value for Φ_V because it is derived assuming $\Phi_D = 0$ and $\Phi_N = 0$ with lobe reconnection voltages lower than Φ_V. There are reasons to believe none of these assumptions is valid. Firstly, it has been shown from outward fluxes of ionospheric ion species that opening of field lines continues between the magnetic cusps at a low level even when the IMF points northward (*Chandler et al.*, 1999; *Fuselier et al*., 2000) and observations of simultaneous "double" cusps have been interpreted as subsolar reconnection continuing even though the IMF is northward and lobe reconnection is simultaneously taking place (*Lockwood and Moen*, 1999; *Pitout et al.*, 2002;

Lockwood et al., 2003). Thus far we have only a limited number of such observations and so cannot say how common this situation is. Hence, although Φ_D is small during northward IMF, it may be larger than zero some or all of the time. Secondly, as pointed out by *Lockwood* (2019), the tail lobes have never been seen to vanish, no matter how long the IMF remains northward. This means there is always a cross-tail current sheet with magnetic shear across it at which we would expect nightside reconnection to occur, even if the resulting Φ_N is small. Thirdly *Wilder et al.* (2008) use SuperDARN data to show that the lobe reconnection voltages in the ionosphere saturates at about 15-20 kV and hence the voltages seen at large times since the IMF turned northward are likely to be caused by lobe reconnection than by viscous-like interaction.

Our definition of Φ_{PC} means that a lobe reconnection Φ_V would, if large enough either increase (the "hybrid" case) or set the value of Φ_{PC} (the lobe-dominated case) such that its effect in the ionosphere exceeded Φ_V (see section 1-i). Figure 7 shows that northward IMF Φ_{PC} increases up to 15kV as the IMF approaches its largest positive values which is a behaviour expected of Φ_L rather than Φ_V. Hence the 15kV is consistent with being a "lobe dominated" Φ_{PC} value set by lobe reconnection and not a "conventional" or "hybrid" viscous-like voltage to which Φ_V could have contributed. As a consequence, we must treat 15 kV as an upper limit to the average value of Φ_V and it is very likely to be considerably lower than this.

4-iii. The effect of dynamic pressure

There are physical reasons to expect both the Φ_D and Φ_N to be increased by increased solar wind dynamic pressure p_{SW}. In both cases, the compression brought about by greater p_{SW} should increase the magnetic shear across the current sheet and so enhance the reconnection rate. One caveat to this idea is that the nightside reconnection must be taking place at a GSM X-coordinate at which the tail is still flaring (i.e., the radius increases with increasingly negative X) and so the dynamic pressure can squeeze the tail lobe and so increase the lobe field (*Caan et al*., 1973) and the cross-tail current (*Lockwood*, 2013). At larger $-X$ coordinates, further down the tail, the tail radius asymptotically reaches its maximum value and the component of the dynamic pressure perpendicular to the magnetopause falls to zero: in this case, the lobe field and magnetic shear across the cross-tail current sheet are set by the static pressure in the interplanetary medium.

Using the *am* geomagnetic index as a proxy indicator of magnetopause reconnection, *Scurry and Russell* (1991) inferred statistically that dayside reconnection voltage Φ_D was indeed enhanced by increased p_{SW}. However much of the evidence for such an effect comes from transient responses to individual events in which p_{SW} increases suddenly (e.g., *Boudouridis et al*., 2003). The problem with these events is there will be a number of transient responses, of which the effect of p_{SW} on Φ_D is one and isolating just that one effect is difficult.

An important effect of p_{SW} on the tail was demonstrated directly by *Karlsson et al.* (2000) who showed that near-Earth tail energy content was reduced if p_{SW} decreased and that such sudden decreases caused quenching of any substorm expansion that had recently begun. This strongly suggests reduced p_{SW} can reduce the nightside voltage, Φ_N. Conversely, increases in p_{SW} have been seen to trigger onsets of full substorm expansion phases (*Schieldge and Siscoe*, 1970; *Kokubun et al.*, 1977; *Yue et al.*, 2010) and have been identified as a cause of a rise in Φ_N (*Boudouridis et al*., 2008b). In some cases, the rise in Φ_N has been inferred from a loss of open flux as aurora expands into what appears to be open flux (*Hubert et al*., 2006a).

Various observational studies suggest that increases in p_{SW} cause enhanced general magnetospheric convection and field-aligned current systems as well as enhanced geomagnetic activity (e.g., *Lukianova*, 2003; *Lee et al*., 2004; *Hubert et al*., 2006b; *Boudouridis et al*., 2008a, *Stauning & Troshichev*, 2008). This phenomenon has been modelled using global MHD models of the magnetosphere as being caused by rises in both Φ_D *and* Φ_N (*Palmroth et al*., 2004; *Ober et al.*, 2006; *Connor et al.*, 2014; *Lockwood et al.*, 2020b).

Figure 15 looks at the implications for any influence of p_{SW} on Φ_D and Φ_N of the correlations between p_{SW} and the auroral electrojet indices for both northward and southward IMF. It also compares the correlograms with those for p_{SW} and Φ_{PC} for northward and southward IMF that were shown in Figure 6. The blue and orange and lines are for AU and AL, respectively, for southward IMF ($B_Z < 0$). Both show a rapid response, although the correlation does not decay away for large positive lags as quickly for AU as it does for AL. Note that correlations are lower for the southward IMF data than for northward IMF (shown by the mauve and green lines) because the controlling influence of IMF B_Z is much greater for southward IMF. The mauve and green lines are for AU and AL, respectively and for northward IMF we see that AL responds to p_{SW} after a long lag, consistent with the squeezing of the tail by increased p_{SW}

increasing Φ_N. From the peak correlation this appears to be a relatively weak effect compared to the peaks for AU: however, it must be remembered that the lag for the dayside effect is short and much less variable than for any effect on the nightside and so we should expect a broad, but relatively low, peak for the effect on AL. Also note the peak for AU at short lags for northward IMF implies that the dayside reconnection is not only enhanced by increased p_{SW} when the IMF is southward, but that it may still present and enhanced by p_{SW} when it is IMF is northward. *Finch et al*. (2008) and *Lockwood et al*. (2020a) found that the effect of p_{SW} on mid-latitude range indices was via the nightside substorm current wedge. These authors also showed the effect was associated with Φ_N and was the origin of the equinoctial time-of-day/time-of-year pattern in geomagnetic activity via the effect of the dipole tilt. The modelling analysis of *Lockwood et al.* (2020b) found both influence of p_{SW} via both Φ_N and the energy stored in the tail lobe. The results presented here show an effect of p_{SW} on Φ_{PC}, but that the effect is smaller than for am: this indicates that the effect of energy stored in the tail may be a larger factor for mid-latitude range indices such as am .

Since submitting the present paper, an article by *Boudouridis et al.*, (2021) has been published, presenting an observation and modelling case study on enhancements in Φ_D *and* Φ_N, and hence Φ_{PC}, induced by enhanced p_{SW}. As mentioned above, the studies of transient responses do not necessarily reveal the dependence of Φ_D *and* Φ_N , and hence Φ_{PC}, on p_{SW} because of other transient responses although they do show a connection. We here have shown that there is a connection on a statistical basis. One potential problem is that p_{SW} has many parameters in common with the power input into the magnetosphere, but *Lockwood et al.* (2020a; b, 2021) have demonstrated that it has a separate and distinct influence on the am mid-latitude, range geomagnetic activity index. We here have demonstrated that p_{SW} has a similar influence on the nightside auroral AL index and the transpolar voltage Φ_{PC}.

Acknowledgements. The authors acknowledge the use of data from the SuperDARN project. SuperDARN is a collection of radars funded by national scientific funding agencies of Australia, Canada, China, France, Italy, Japan, Norway, South Africa, United Kingdom and the United States of America. The work presented in this paper was supported by a number of grants. ML is supported by STFC consolidated grant number ST/M000885/1 and by the

SWIGS NERC Directed Highlight Topic Grant number NE/P016928/1/. Funding for KAM at University of Saskatchewan was provided by the Canadian Foundation for Innovation (CFI), the Province of Saskatchewan, and a Discovery Grant from the Natural Sciences and Engineering Research Council (NSERC) of Canada. Initial work by KAM for this paper was carried out at University of Reading on sabbatical leave from University of Saskatchewan. We thank Evan Thomas, Kevin Sterne, Simon Shepherd, Keith Kotyk, Marina Schmidt, Pasha Ponomarenko, Emma Bland, Maria-Theresia Walach, Ashton Reimer, Angeline Burrell, and Daniel Billett for the SuperDARN radar processing toolkit used to analyse the radar data. The authors are also grateful to the staff of: the Space Physics Data Facility, NASA/Goddard Space Flight Center, who prepared and made available the OMNI2 dataset used: these interplanetary data were downloaded from http://omniweb.gsfc.nasa.gov/ow.html; the World Data Center for Geomagnetism, Kyoto who generate and make available the *AL* index from http://wdc.kugi.kyoto-u.ac.jp/aeasy/index.html and the staff of L'École et Observatoire des Sciences de la Terre (EOST), a joint of the University of Strasbourg and the French National Center for Scientific Research (CNRS) and the International Service of Geomagnetic Indices (ISGI) for making the am index data available from http://isgi.unistra.fr/data_download.php

References

Aikio, A., Pitkänen, T., Honkonen, I., Palmroth, M., Amm, O. (2013) IMF effect on the polar cap contraction and expansion during a period of substorms, *Annales Geophysicae*, **31**: 1021-1034 , doi: 10.5194/angeo-31-1021-2013

Baker, D. N., Klimas, A. J., Vassiliadis, D., Pulkkinen, T. I., and McPherron, R. L. (1997), Re-examination of driven and unloading aspects of magnetospheric substorms, J. *Geophys. Res.*, 102 (A4), 7169– 7177, doi: 10.1029/96JA02627.

Baker, D. N., Zwickl, R. D., Bame, S. J., Hones, E. W., Tsurutani, B. T., Smith, E. J., and Akasofu, S.-I. (1983), An ISEE 3 high time resolution study of interplanetary parameter correlations with magnetospheric activity, *J. Geophys. Res.*, **88** (A8), 6230– 6242, doi:10.1029/JA088iA08p06230.

Birn, J., Hones, E. W., Craven, J. D., Frank, L. A., Elphinstone, R. D., and Stern, D. P. (1991), On open and closed field line regions in Tsyganenko's field model and their possible associations with horse collar auroras, *J. Geophys. Res.*, **96** (A3), 3811– 3817, doi: 10.1029/90JA02124.

Boudouridis, A., L.R. Lyons, E. Zesta, and J. M. Ruohoniemi (2007), Dayside reconnection enhancement resulting from a solar wind dynamic pressure increase, *J. Geophys. Res*., **112**, A06201, doi:10.1029/2006JA012141.

Boudouridis, A., E. Zesta, L. R. Lyons, P. C. Anderson, and A. J. Ridley (2008a), Temporal evolution of the transpolar potential after a sharp enhancement in solar wind dynamic pressure, *Geophys. Res. Lett*., **35**, L02101, doi:10.1029/2007GL031766.

Boudouridis, A., L. R. Lyons, E. Zesta, J. M. Ruohoniemi, and D. Lummerzheim (2008b), Nightside flow enhancement associated with solar wind dynamic pressure driven reconnection, *J. Geophys. Res*., **113**, A12211, doi:10.1029/2008JA013489.

Boudouridis, A., Connor, H. K., Lummerzheim, D., Ridley, A. J., & Zesta, E. (2021). Changes in the Magnetic Field Topology and the Dayside/Nightside Reconnection Rates in Response to a Solar Wind Dynamic Pressure Front: A Case Study. *Journal of Geophysical Research: Space Physics*, **126**, e2020JA028768. doi: 10.1029/2020JA028768

Boyle, C. B., Reiff, P. H., and Hairston, M. R. (1997), Empirical polar cap potentials, *J. Geophys. Res*., **102** (A1), 111– 125, doi: 10.1029/96JA01742.

Bristow, W. A., R. A. Greenwald, S. G. Shepherd, and J. M. Hughes (2004), On the observed variability of the cross–polar cap potential, *J. Geophys. Res*., **109**, A02203, doi: 10.1029/2003JA010206.

Browett, S.D., Fear, R. C., Grocott, A., and Milan, S. E. (2017), Timescales for the penetration of IMF By into the Earth's magnetotail, *J. Geophys. Res. Space Physics*, **122,** 579– 593, doi: 10.1002/2016JA023198.

Caan M.N., McPherron R.L., Russell C.T. (1973), Solar wind and substorm-related changes in the lobes of the geomagnetic tail. *J. Geophys. Res.*,**78** (34): 8087–8096. doi: 10.1029/ja078i034p08087.

Chandler, M.O., S.A. Fuselier, M. Lockwood and T.E. Moore (1999), Evidence of component magnetic merging equatorward of the cusp, *J. Geophys. Res*., **104,** 22623-22648, doi: 10.1029/1999JA900175.

Chen, Y.-J., & Heelis, R. A. (2018). Motions of the convection reversal boundary and local plasma in the high-latitude ionosphere, *Journal of Geophysical Research: Space Physics*,**123**, 2953–2963. doi: 10.1002/2017JA024934

Chisham, G., Lester, M., Milan, S. E., Freeman, M. P., Bristow, W. A., Grocott, A., McWilliams, K. A., Ruohoniemi, J. M., Yeoman, T. K., Dyson, P. L., Greenwald, R. A., Kikuchi, T., Pinnock, M., Rash, J. P. S., Sato, N., Sofko, G.J., Villain, J.-P., Walker, A. D. M. (2007), A decade of the Super Dual Auroral Radar Network (SuperDARN): scientific achievements, new techniques and future directions, *Surveys in Geophys*., **28** (1), 33-109, doi: 10.1007/s10712-007-9017-8.

Connor, H. K., E. Zesta, D. M. Ober, and J. Raeder (2014), The relation between transpolar potential and reconnection rates during sudden enhancement of solar wind dynamic pressure:

OpenGGCM-CTIM results, *J. Geophys. Res. Space Physics*, **119**, 3411–3429, doi: 10.1002/2013JA019728.

Consolini, G., and De Michelis, P. (2005), Local intermittency measure analysis of AE index: The directly driven and unloading component, *Geophys. Res. Lett.*, **32**, L05101, doi:10.1029/2004GL022063.

Cousins, E. D. P., Matsuo, T., and Richmond, A. D. (2013), SuperDARN assimilative mapping, *J. Geophys. Res. Space Physics*, **118**, 7954– 7962, doi:10.1002/2013JA019321.

Cowley, S. W. H. (1982), The causes of convection in the Earth's magnetosphere: A review of developments during the IMS, *Rev. Geophys.*, **20** (3), 531– 565, doi:10.1029/RG020i003p00531.

Cowley, S.W.H. (1984), Solar wind control of magnetospheric convection. *Achievements of the International Magnetospheric Study (IMS)*, Proceedings of an International Symposium, Graz, Austria, 26-28 June 1984, **ESA-SP-*217***, Eds. B. Battrick and E.J. Rolfe., p.483, European Space Agency. ISSN 0379-6566

Cowley, S. W. H., and Lockwood, M. (1992), Excitation and decay of solar-wind driven flows in the magnetosphere-ionosphere system, *Annales Geophys.*, **10**, 103-115.

Cowley, S.W.H., Freeman, M.P., Lockwood, M. and Smith, M.F. (1991a) The ionospheric signature of flux transfer events, in "*CLUSTER - dayside polar cusp*", ed. C.I. Barron, ESA SP-330, 105-112, European Space Agency Publications, Nordvijk, The Netherlands

Cowley, S.W.H., J.P. Morelli, and M. Lockwood (1991b) Dependence of convective flows and particle precipitation in the high-latitude dayside ionosphere on the X and Y components of the interplanetary magnetic field, *J. Geophys. Res.*, **96**, 5557-5564, doi: 10.1029/90JA02063.

Davis, T. N., and Sugiura, M. (1966), Auroral electrojet activity index AE and its universal time variations, *J. Geophys. Res.*, **71** (3), 785–801, doi:10.1029/JZ071i003p00785.

DeJong, A. D., Ridley, A. J., and Clauer, C. R. (2008), Balanced reconnection intervals: four case studies, *Ann. Geophys.*, **26**, 3897–3912, doi: 10.5194/angeo-26-3897-2008, 2008.

Drayton, R. A., Koustov, A. V., Hairston, M. R., and Villain, J.-P. (2005), Comparison of DMSP cross-track ion-drifts and SuperDARN line-of-sight velocities, *Annales Geophysicae*, **23** (7), 2479–2486, doi: 10.5194/angeo-23-2479-2005.

Echer, E., Korth, A., Bolzan, M. J. A., & Friedel, R. H. W. (2017), Global geomagnetic responses to the IMF B_z fluctuations during the September/October 2003 high-speed stream intervals, *Annales Geophys.*, **35** (4), 853-868, doi: 10.5194/angeo-35-853-2017.

Etemadi, A., Cowley, S. W. H., Lockwood, M., Bromage, B. J. I., Willis, D. M. and Lühr, H. (1988), The dependence of high-latitude dayside ionospheric flows on the north-south component of the IMF: a high time resolution correlation analysis using EISCAT "POLAR" and AMPTE UKS and IRM data, *Planet. Space Sci.*, **36**, 471-498, doi: 10.1016/0032-0633(88)90107-9.

994 Farrugia, C.J., Gratton, F.T. & Torbert, R.B (2001), Viscous-type processes in the solar wind-
995 magnetosphere interaction. *Space Science Reviews* 95, 443–456. doi:
996 10.1023/A:1005288703357

997 Finch, I. D., Lockwood, M., and Rouillard, A. P. (2008), The effects of solar wind
998 magnetosphere coupling recorded at different geomagnetic latitudes: separation of directly-
999 driven and storage/release systems, *Geophys. Res. Lett*., **35**, L21105,
1000 doi:10.1029/2008GL035399.

1001 Fuselier, S.A., M. Lockwood, T.G. Onsager and W.K. Peterson (1999) The source population
1002 for the cusp and cleft/LLBL for southward IMF, *Geophys. Res. Lett*., **26**, 1665-1669, doi:
1003 10.1029/1999GL900354.

1004 Fuselier, S.A., Trattner, K. J., and Petrinec, S. M. (2000), Cusp observations of high- and low-
1005 latitude reconnection for northward interplanetary magnetic field, *J. Geophys. Res*., **105** (A1),
1006 253– 266, doi:10.1029/1999JA900422.

1007 Greenwald, R. A., Bristow, W. A., Sofko, G. J., Senior, C., Ceriser, J.-C., and Szabo, A.
1008 (1995), Super Dual Auroral Radar Network radar imaging of dayside high-latitude convection
1009 under northward interplanetary magnetic field: toward resolving the distorted two-cell versus
1010 multicell controversy, *J. Geophys. Res.*, **100**, 19661–19674, doi: 10.1029/95ja01215.

1011 Gao, Y. (2012), Comparing the cross polar cap potentials measured by SuperDARN and
1012 AMIE during saturation intervals, *J. Geophys. Res*., **117**, A08325, doi:
1013 10.1029/2012JA017690.

1014 Gordeev, E. I., Sergeev, V. A., Pulkkinen, T. I., and Palmroth, M. (2011), Contribution of
1015 magnetotail reconnection to the cross-polar cap electric potential drop, *J. Geophys. Res.*, **116**,
1016 A08219, doi:10.1029/2011JA016609.

1017 Haines, C. A., Owens, M. J., Barnard, L. A., Lockwood, M., and Ruffenach, A. (2019) The
1018 variation of geomagnetic storm duration with intensity, *Solar Physics*, **294**, 154, pp1-15, doi:
1019 10.1007/s11207-019-1546-z.

1020 Hairston, M. R., Heelis, R. A., and Rich, F. J. (1998), Analysis of the ionospheric cross polar
1021 cap potential drop using DMSP data during the National Space Weather Program study
1022 period, *J. Geophys. Res.*, **103** (A11), 26337– 26347, doi: 10.1029/97JA03241.

1023 Hanson, W. B., Coley, W. R., Heelis, R. A., Maynard, N. C., and Aggson, T. L. (1993), A
1024 Comparison of in situ measurements of $\vec{E}$ and $-\vec{V}\times\vec{B}$ from Dynamics Explorer 2, *J. Geophys.*
1025 *Res.*, **98** (A12), 21501– 21516, doi:10.1029/93JA01422.

1026 Hapgood, M.A., and M. Lockwood (1993) On the voltage and distance across the low-latitude
1027 boundary layer, *Geophys. Res. Lett*., **20**, 145-148, doi: 10.1029/93GL00063

1028 Hapgood, M. A., Bowe, G., Lockwood, M., Willis, D. M., and Tulunay, Y. (1991) Variability
1029 of the interplanetary magnetic field at 1 A.U. over 24 years: 1963 – 1986, *Planet. Space Sci.*,
1030 **39**, 411-423, doi: 10.1016/0032-0633(91)90003-S.

Holzer, R. E., McPherron, R. L., and Hardy, D. A. (1986), A quantitative empirical model of the magnetospheric flux transfer process, *J. Geophys. Res.*, **91**(A3), 3287– 3293, doi:10.1029/JA091iA03p03287.

Hones, E.W. Jr., J. D. Craven, L. A. Frank, D. S. Evans, P. T. Newell (1989) The horse-collar aurora: A frequent pattern of the aurora in quiet times, *Geophys. Res. Lett*., **16** (1), 37-40, doi: 10.1029/GL016i001p00037

Huang, C.-S., A. D. DeJong, and X. Cai (2009), Magnetic flux in the magnetotail and polar cap during sawteeth, isolated substorms, and steady magnetospheric convection events, *J. Geophys. Res*., **114**, A07202, doi: 10.1029/2009JA014232.

Hubert, B., M. Palmroth, T. V. Laitinen, P. Janhunen, S. E. Milan, A. Grocott, S. W. H. Cowley, T. Pulkkinen, and J.-C. Gérard (2006a), Compression of the Earth's magnetotail by interplanetary shocks directly drives transient magnetic flux closure, *Geophys. Res. Lett*., **33**, L10105, doi:10.1029/2006GL026008

Hubert, B., Milan, S. E., Grocott, A., Block, C., Cowley, S. W. H., and Gérard, J.-C. (2006b), Dayside and nightside reconnection rates inferred from IMAGE FUV and Super Dual Auroral Radar Network data, *J. Geophys. Res*., **111**, A03217, doi:10.1029/2005JA011140

Imber, S. M., Milan, S. E., and Lester, M. (2013) Solar cycle variations in polar cap area measured by the superDARN radars, *Journal of Geophysical Research: Space Physics*, **118** (10), 6188 – 6196, doi: 10.1002/jgra.50509.

Karlsson, S.B.P., Opgenoorth, H.J., Eglitis, P., Kauristie, K, Syrjäsuo, M., Pulkkinen, T.I., Lockwood, M., Nakamura, R., Reeves, G., Romanov, S. (2000) Solar wind control of magnetospheric energy content: substorm quenching and multiple onsets. *J. Geophys. Res*., **105**, 5335-5356, doi: 10.1029/1999JA900297

King, J.H. and N.E. Papitashvili (2005) Solar wind spatial scales in and comparisons of hourly Wind and ACE plasma and magnetic field data, *J. Geophys. Res*.,**110**, A02104, doi: 10.1029/2004JA010649

Kokubun S. McPherron, R.L. Russell, C.T. (1977) Triggering of substorms by solar wind discontinuities. *J. Geophys. Res*., **82** (1) 74-86, doi: 10.1029/ja082i001p00074.

Klimas, A. J., Baker, D. N., Vassiliadis, D., and Roberts, D. A. (1994), Substorm recurrence during steady and variable solar wind driving: *Evidence* for a normal mode in the unloading dynamics of the magnetosphere, *J. Geophys. Res*., **99**, 14855–14861. doi: 10.1029/94JA01240.

Koustov, A. V., Lavoie, D. B., Kouznetsov, A. F., Burchill, J. K., Knudsen, D. J., & Fiori, R. A. D. (2019a), A comparison of cross-track ion drift measured by the Swarm satellites and plasma convection velocity measured by SuperDARN, *Journal of Geophysical Research: Space Physics*,**124**, 4710–4724, doi: 10.1029/2018JA026245

Koustov, A. V., Ullrich, S., Ponomarenko, P. V., Nishitani, N., Marcucci, F. M., Bristow, W. A. (2019b), Occurrence of F region echoes for the polar cap SuperDARN radars, *Earth Planets Space*, **71**, 112 (2019b). doi: 10.1186/s40623-019-1092-9

Kubota, Y., Nagatsuma, T., Den, M., Tanaka, T., and Fujita, S. (2017), Polar cap potential saturation during the Bastille Day storm event using global MHD simulation, *J. Geophys. Res. Space Physics*, **122**, 4398–4409, doi:10.1002/2016JA023851.

Laundal, K.M., Reistad, J.P., Hatch, S.M. et al. (2020) Time-scale dependence of solar wind-based regression models of ionospheric electrodynamics. *Sci. Rep.* **10**, 16406. doi: 10.1038/s41598-020-73532-z

Lee D.-Y., Lyons L.R., Yumoto K. (2004), Sawtooth oscillations directly driven by solar wind dynamic pressure enhancements, *J. Geophys. Res*., **109**, A04202. doi: 10.1029/2003JA010246.

Lockwood, M. (1991), On flow reversal boundaries and cross-cap potential in average models of high latitude convection, *Planet. Space Sci*., **39**, 397-409, doi: 10.1016/0032-0633(91)90002-R.

Lockwood, M. (2013) Reconstruction and Prediction of Variations in the Open Solar Magnetic Flux and Interplanetary Conditions, *Living Reviews in Solar Physics*, **10**, 4, 2013. doi: 10.12942/lrsp-2013-4

Lockwood, M. (2019), Does adding solar wind Poynting flux improve the optimum solar wind-magnetosphere coupling function? *J. Geophys. Res. (Space Physics),* **124** (7), 5498-5515, doi: 10.1029/2019JA026639.

Lockwood, M., and Cowley, S.W.H. (1992) Ionospheric Convection and the substorm cycle in "Substorms 1, Proceedings of the First International Conference on Substorms, ICS-1", ed C. Mattock, ESA-SP-335, 99-109, European Space Agency Publications, Nordvijk, The Netherlands.

Lockwood M. and M.A. Hapgood (1997) How the Magnetopause Transition Parameter Works, *Geophys. Res. Lett*., **24**, 373-376, doi: 10.1029/97GL00120

Lockwood, M., and Moen, J. (1999) Reconfiguration and closure of lobe flux by reconnection during northward IMF: evidence for signatures in cusp/cleft auroral emissions, *Annales Geophys*., **17**, 996-1011, doi: 10.1007/s00585-999-0996-2.

Lockwood, M., and Morley, S. E. (2004), A numerical model of the ionospheric signatures of time-varying magnetic reconnection: I. Ionospheric convection, *Annales Geophys*., **22**, 73-91, doi: 10.5194/angeo-22-73-2004.

Lockwood, M., van Eyken, A. P., Bromage, B. J. I., Willis, D. M., and Cowley, S. W. H. (1986), Eastward propagation of a plasma convection enhancement following a southward turning of the interplanetary magnetic field, *Geophys. Res. Lett*., **13**, 72-75, doi: 10.1029/GL013i001p00072.

Lockwood, M., S.W.H. Cowley, H. Todd, D.M. Willis and C.R. Clauer (1988) Ion flows and heating at a contracting polar cap boundary, *Planet. Space Sci.*, **36**, 1229-1253, doi: 10.1016/0032-0633(88)90076-1

Lockwood, M., Cowley, S. W. H., and Freeman, M. P. (1990), The excitation of plasma convection in the high latitude ionosphere, *J. Geophys Res.*, **95**, 7961-7971, doi: 10.1029/JA095iA06p07961, 1990

Lockwood, M., Denig, W.F., Farmer, A.D., Davda, V.N., Cowley, S.W.H and Lühr, H. (1993) Ionospheric signatures of pulsed magnetic reconnection at the Earth's magnetopause, *Nature*, **361** (6411), 424-428. doi: 10.1038/361424a0

Lockwood, M., B.S. Lanchester, H. Frey, K. Throp, S. Morley, S.E. Milan, and M.E. Lester (2003) IMF Control of Cusp Proton Emission Intensity and Dayside Convection: implications for component and anti-parallel reconnection, *Annales Geophys.*, **21**, 955 982, doi: 10.5194/angeo-21-955-2003

Lockwood, M., Throp, K. Lanchester, B. S., Morley, S. K., Milan, S. E., Lester, M., and H. U. Frey, H. U. (2006), Modelling the observed proton aurora and ionospheric convection responses to changes in the IMF field clock angle: 2. The persistence of ionospheric convection, *J. Geophys. Res.*, **111**, A02306, doi:10.1029/2003JA010307.

Lockwood, M., Hairston, M. R., Finch, I. D., and Rouillard, A. P. (2009), Transpolar voltage and polar cap flux during the substorm cycle and steady convection events, *J. Geophys. Res.*, **114**, A01210, doi: 10.1029/2008JA013697.

Lockwood, M., Owens, M. J., Barnard, L. A., Bentley, S., Scott, C. J., and Watt, C. E. (2016), On the Origins and Timescales of Geoeffective IMF, *Space Weather,* **14**, 406 432, doi: 10.1002/2016SW001375.

Lockwood, M., Owens, M. J., Barnard, L. A., Scott, C. J., and Watt, C. E. (2017), Space Climate and Space Weather over the past 400 years: 1. The Power input to the Magnetosphere, *J. Space Weather Space Clim.*, **7**, A25, doi: 10.1051/swsc/2017019.

Lockwood, M., Chambodut, A., Barnard, L. A., Owens, M. J., Clarke, E., and Mendel, V. (2018a), A homogeneous aa index: 1. Secular variation, *J. Space Weather Space Clim.*, **8**, A53, doi: 10.1051/swsc/2018038.

Lockwood, M., Finch, I. D., Chambodut, A., Barnard, L. A., Owens, M. J., and Clarke, E. (2018b), A homogeneous aa index: 2. hemispheric asymmetries and the equinoctial variation, *J. Space Weather Space Clim.*, **8**, A58, doi: 10.1051/swsc/2018044.

Lockwood, M., Bentley, S., Owens, M. J., Barnard, L. A., Scott, C. J., Watt, C. E. and Allanson, O. (2019a), The development of a space climatology: 1. Solar-wind magnetosphere coupling as a function of timescale and the effect of data gaps, *Space Weather*, 17, 133-156, doi: 10.1029/2018SW001856.

Lockwood, M., S. Bentley, M.J. Owens, L.A. Barnard, C.J. Scott, C.E. Watt, O. Allanson and M.P. Freeman (2019b) The development of a space climatology: 2. The distribution of power input into the magnetosphere on a 3-hourly timescale, *Space Weather*, **17**, 157-179. doi: 10.1029/2018SW002016

Lockwood, M., S. Bentley, M.J. Owens, L.A. Barnard, C.J. Scott, C.E. Watt, O. Allanson and M.P. Freeman (2019c) The development of a space climatology: 3. The evolution of

distributions of space weather parameters with timescale, *Space Weather*, **17**, 180-209. doi: 10.1029/2018SW002017

Lockwood, M., K.A. McWilliams, M.J. Owens, L.A. Barnard, C.E. Watt, C.J. Scott, A. McNeill and J.C. Coxon (2020a) Semi-annual, annual and Universal Time variations in the magnetosphere and in geomagnetic activity: 2. Response to solar wind power input and relationships with solar wind dynamic pressure and magnetospheric flux transport, *J. Space Weather Space Clim.*, **10**, 30, doi: 10.1051/swsc/2020033

Lockwood, M., M.J. Owens, L.A. Barnard, C.E. Watt, C.J. Scott, J.C. Coxon and K.A. McWilliams (2020b) Semi-annual, annual and Universal Time variations in the magnetosphere and in geomagnetic activity: 3. Modelling, *J. Space Weather and Space Climate*, **10**, 61 doi: 10.1051/swsc/2020062

Lockwood, M., C.A. Haines, L.A. Barnard, J. Owens, C.J. Scott, A. Chambodut, and K.A. McWilliams (2021) Semi-annual, annual and Universal Time variations in the magnetosphere and in geomagnetic activity: 4. Polar Cap motions and origins of the Universal Time effect, *J. Space Weather and Space Climate*, **11**, 15, doi: 10.1051/swsc/2020077

Lopez, R. E., Wiltberger, M., Lyon, J. G., Goodrich, C. C., Papadopoulos, K. (1999) MHD simulations of the response of high-latitude potential patterns and polar cap boundaries to sudden southward turnings of the interplanetary magnetic field, *Geophys. Res. Lett.*, **26** (7), 967 – 970, doi: 10.1029/1999GL900113.

Lopez, R. E., Lyon, J. G., Wiltberger, M. J., Goodrich, C. C. (2001) Comparison of global MHD simulation results with actual storm and substorm events, Adv. *Space Res.*, **28**, (12), 1701-1706, doi: 10.1016/S0273-1177(01)00535-X

Lühr, H., M. Lockwood, P.A. Sandholt, T.L. Hansen and T. Moretto (1996) Multi-instrument ground-based observations of a Travelling Convection Vortex event, *Annales Geophys.*, **14**, 162-181, doi: 10.1007/s00585-996-0162-z.

Liu, E., H. Hu, J. Liu, X. Teng, L. Qiao (2019) Predicting SuperDARN cross polar cap potential by applying regression analysis and machine learning, *J. Atmos. Sol.-Terr. Phys.*, **193**, 105057, doi: 10.1016/j.jastp.2019.105057.

Lukianova R. (2003), Magnetospheric response to sudden changes in solar wind dynamic pressure inferred from polar cap index, *J. Geophys. Res.*, **108**(A12), 1428 doi: 10.1029/2002JA009790.

Mayaud, P.-N. (1980), Derivation, Meaning and Use of Geomagnetic Indices, *Geophysical Monograph, 22*, American Geophysical Union, Washington, DC. doi: 10.1029/GM022.

McPherron, R. L. (2020), Early studies in solar wind coupling and substorms, *Journal of Geophysical Research: Space Physics*, 125, e2019JA027615, doi: 10.1029/2019JA027615.

McPherron, R.L., Baker, D. N., Bargatze, L. F., Clauer, C. R., and Holzer, R. E. (1998), IMF control of geomagnetic activity, *Adv. Space Res.*, **8** (9–10), 71-86, doi: 10.1016/0273-1177(88)90114-7.

McWilliams, K.A., Yeoman, T. K., and Cowley, S. W. H (2000) Two-dimensional electric field measurements in the ionospheric footprint of a flux transfer event, *Annales Geophys*., **18** (12), 1584 -1598. doi: 10.1007/s00585-001-1584-2

McWilliams, K. A., Pfeifer, J. B., and McPherron, R. L. (2008), Steady magnetospheric convection selection criteria: Implications of global SuperDARN convection measurements, *Geophys. Res. Lett*., **35**, L09102, doi:10.1029/2008GL033671.

Milan, S. E. (2004), Dayside and nightside contributions to the cross polar cap potential: placing an upper limit on a viscous-like interaction, *Ann. Geophys*., **22**, 3771–3777, doi: 10.5194/angeo-22-3771-2004.

Milan, S. E., Lester, M., Cowley, S. W. H. Oksavik, K., Brittnacher, M., Greenwald, R. A., Sofko, G., and Villain, J.-P. (2003), Variations in the polar cap area during two substorm cycles, *Annales Geophys*., **21** (5),1121-1140, doi: 10.5194/angeo-21-1121-2003.

Milan, S. E., Hutchinson, J., Boakes, P. D., and Hubert, B. (2009), Influences on the radius of the auroral oval, *Annales Geophys*, **21** (5), 1121-1140. doi: 10.5194/angeo-21-1121-2003.

Milan, S. E., Gosling, J. S., and Hubert, B. (2012), Relationship between interplanetary parameters and the magnetopause reconnection rate quantified from observations of the expanding polar cap, *J. Geophys. Res*., **117**, A03226, doi: 10.1029/2011JA017082.

Milan, S. E., Carter, J. A., Bower, G. E., Imber, S. M., Paxton, L. J., Anderson, B. J., et al. (2020). Dual-lobe reconnection and horse-collar auroras. *Journal of Geophysical Research: Space Physics*, **125**, e2020JA028567. doi: 10.1029/2020JA028567

Milan, S. E., Carter, J. A., Sangha, H., Bower, G. E., & Anderson, B. J. (2021). Magnetospheric flux throughput in the Dungey cycle: Identification of convection state during 2010. *Journal of Geophysical Research: Space Physics*, **126**, e2020JA028437. doi: 10.1029/2020JA028437

Mishin V. V. Karavaev Yu. A. (2017) Saturation of the magnetosphere during superstorms: new results from the magnetogram inversion technique, *Solar-Terrestrial Physics*, **3** (3), 28-36, doi: 10.12737/stp-33201704

Morley, S. E., and Lockwood, M. (2005), A numerical model of the ionospheric signatures of time-varying magnetic reconnection: II. Measuring expansions in the ionospheric flow response, *Annales Geophys.*, **23**, 2501-2510, doi: 10.5194/angeo-23-2501-2005

Mozer, F.S. (1984), Electric field evidence on the viscous interaction at the magnetopause. *Geophys. Res. Lett.,* **11**, 135-138. doi: 10.1029/GL011i002p00135

Mozer, F.S., H. Hayakawa, S. Kokubun, M. Nakamura, T. Okada, T. Yamamoto and K. Tsuruda (1994) The morningside low-latitude boundary layer as determined from electric and magnetic field measurements on Geotail, *Geophys. Res. Lett.,* **21** (25), 2983-2986, doi: 10.1029/94GL01296

Newell, P. T., W. J. Burke, E. R. Sanchez, et al. (1991), The low-latitude boundary layer and the boundary plasma sheet at low altitude: Prenoon precipitation regions and convection reversal boundaries, *J. Geophys. Res.*, 96, 21,013–21,023, doi: 10.1029/91ja01818

Nishida, A. (1968a), Coherence of geomagnetic DP 2 fluctuations with interplanetary magnetic variations, *J. Geophys. Res.*, **73** (17), 5549– 5559, doi: 10.1029/JA073i017p05549.

Nishida, A. (1968b), Geomagnetic DP 2 fluctuations and associated magnetospheric phenomena, *J. Geophys. Res*., **73** (5), 1795– 1803, doi: 10.1029/JA073i005p01795.

Ober, D. M., G. R. Wilson, N. C. Maynard, W. J. Burke, and K. D. Siebert (2006), MHD simulation of the transpolar potential after a solar-wind density pulse, *Geophys. Res. Lett.*, **539**(33), L04106, doi:10.1029/2005GL024655.

Palmroth, M., Pulkkinen, T.I., Janhunen, P., McComas, D.J., Smith, C.W., Koskinen, H.E.J. (2004), Role of solar wind dynamic pressure in driving ionospheric Joule heating, *J. Geophys. Res.*, **109**, A11302, doi: 10.1029/2004JA010529.

Pitout, F., Newell, P.T. and Buchert, S.C. (2002) Simultaneous high-and low-latitude reconnection: ESR and DMSP observations, *Annales Geophys*., **20** (9), 1311-1320, doi: 10.5194/angeo-20-1311-2002

Provan, G., Yeoman, T. K., Milan, S. E., Ruohoniemi, J. M., and Barnes, R. (2002) An assessment of the ‘‘map-potential’’ and ‘‘beam-swinging’’ techniques for measuring the ionospheric convection pattern using data from the SuperDARN radars, *Annales Geophys*, **20**, 191–202, doi: 10.5194/angeo-20-191-2002.

Reiff, P. H., Spiro, R. W., and Hill, T. W. (1981), Dependence of polar cap potential drop on interplanetary parameters, *J. Geophys. Res*., **86** (A9), 7639– 7648, doi: 10.1029/JA086iA09p07639.

Ruohoniemi, J. M., and Baker K. B, (1998) Large-scale imaging of high-latitude convection with Super Dual Auroral Radar Network HF radar observations, *J. Geophys. Res.*, **103**, 20797–20811, doi: 10.1029/98ja01288.

Saunders, M. A., Freeman, M. P., Southwood, D. J., Cowley, S. W. H., Lockwood, M., Samson, J. C., Farrugia, C. J., and Hughes, T. J. (1992) Dayside ionospheric convection changes in response to long period IMF oscillations: determination of the ionospheric phase velocity, *J. Geophys. Res*., **97**, 19373-19380, doi: 10.1029/92JA01383.

Schieldge, J.P., Siscoe, G.L. (1970) A correlation of the occurrence of simultaneous sudden magnetospheric compressions and geomagnetic bay onsets with selected geophysical indices. *J. Atmos. Terr. Phys*., **32** (11), 1819-1830, doi: 10.1016/0021-9169(70)90139-x.

Scurry, L., and Russell, C. T. (1991), Proxy studies of energy transfer to the magnetosphere, *J. Geophys. Res*., **96** (A6), 9541– 9548, doi:10.1029/91JA00569.

Shepherd, S. G., and Ruohoniemi, J. M. (2000), Electrostatic potential patterns in the high-latitude ionosphere constrained by SuperDARN measurements, *J. Geophys. Res*., **105**, 23005–23014, doi: 10.1029/2000ja000171.

1258 Siscoe, G. L., and Huang, T. S. (1985), Polar cap inflation and deflation, *J. Geophys. Res.*, **90**
1259 (A1), 543– 547, doi:10.1029/JA090iA01p00543.

1260 Stauning P., Troshichev, O.A. (2008), Polar cap convection and PC index during sudden
1261 changes in solar wind dynamic pressure, *J. Geophys. Res.*, **113**, A08227, doi:
1262 10.1029/2007JA012783.

1263 Sundberg, K. Å. T., Blomberg, L. G., and Cumnock, J. A. (2008), Statistical analysis of the
1264 sources of the cross-polar potential for southward IMF, based on particle precipitation
1265 characteristics, *Geophys. Res. Lett*., **35**, L08103, doi:10.1029/2008GL033383

1266 Throp, K., M. Lockwood, B. S. Lanchester, S. K. Morley, and H. U. Frey (2005) Modeling
1267 the observed proton aurora and ionospheric convection responses to changes in the IMF clock
1268 angle: 1. Persistence of cusp proton aurora, *J. Geophys. Res.*, **110**, A12311, doi:
1269 10.1029/2003JA010306

1270 Todd, H., Cowley, S. W. H., Etemadi, A., Bromage, B. J. I., Lockwood, M., Willis, D. M.,
1271 and Lühr, H. (1988) Flow in the high-latitude ionosphere: measurements at 15-second
1272 resolution made using the EISCAT "POLAR" experiment, *J. atmos. terr. Phys.*, **50**, 423-446,
1273 doi: 10.1016/0021-9169(88)90026-8.

1274 Weigel, R. S. (2007), Solar wind time history contribution to the day-of-year variation in
1275 geomagnetic activity, *J. Geophys. Res.*, 112, A10207, doi: 10.1029/2007JA012324.

1276 Weimer, D. R., Maynard, N. C., Burke, W. J., & Liebrecht, C. (1990), Polar cap potentials
1277 and the auroral electrojet indices, *Planetary and space science*, **38**(9), 1207-1222. doi:
1278 10.1016/0032-0633(90)90028-o

1279 Wilder, F. D., Clauer, C. R., and Baker, J. B. H. (2008), Reverse convection potential
1280 saturation during northward IMF, *Geophys. Res. Lett*., **35**, L12103,
1281 doi:10.1029/2008GL034040.

1282 Wilder, F. D., Clauer, C. R., Baker, J. B. H., Cousins, E. P., and Hairston, M. R. (2011) The
1283 nonlinear response of the polar cap potential under southward IMF: A statistical view, *J.*
1284 *Geophys. Res.*, **116**, A12229, doi:10.1029/2011JA016924.

1285 Wygant, J. R., Torbert, R. B., and Mozer, F. S. (1983), Comparison of S3-3 polar cap
1286 potential drops with the interplanetary magnetic field and models of magnetopause
1287 reconnection, *J. Geophys. Res.*, **88** (A7), 5727– 5735, doi:10.1029/JA088iA07p05727.

1288 Xu, L., Koustov, A. V. Xu, J. S., Drayton, R. A., and Huo, L. (2007a), A 2-D comparison of
1289 ionospheric convection derived from SuperDARN and DMSP measurements, *Adv. Space*
1290 *Res.*, **42** (7), 1259-1266, doi: 10.1016/j.asr.2007.06.044.

1291 Xu, L., Xu, J., Alexandre, K., Papitashvili, V., and Rich, F. (2007b) A comparison of
1292 SuperDARN-derived plasma convection and DMSP ion drift measurements, *Wuhan Univ. J.*
1293 *of Nat. Sci.*, **12**, 279–283. doi: 10.1007/s11859-006-0024-2

Yue, C., Zong, Q.G., Zhang, H., Wang, Y.F., Yuan, C.J., Pu, Z.Y., Fu, S.Y., Lui, A.T.Y., Yang, B., Wang, C.R. (2010), Geomagnetic activity triggered by interplanetary shocks. *J. Geophys. Res.* **115**, A00I05. doi: 10.1029/2010JA015356.

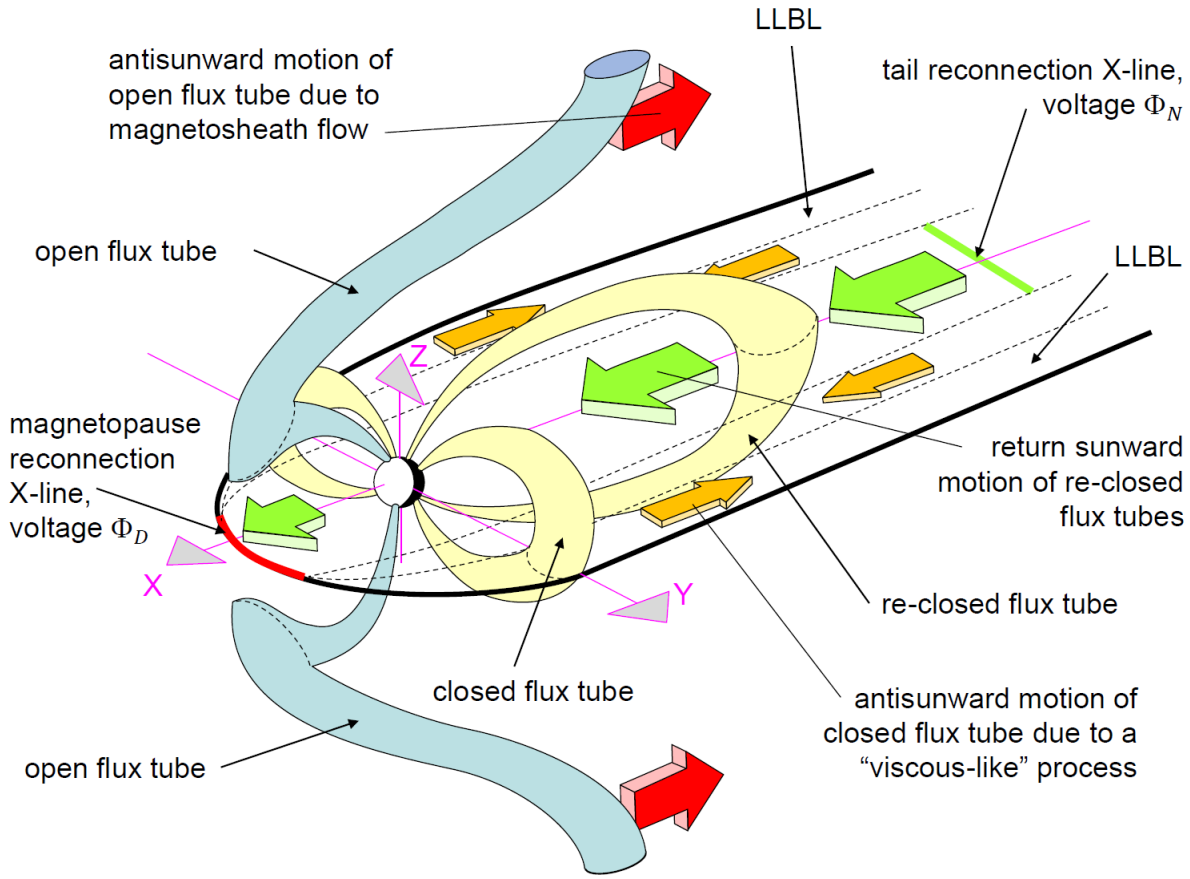

Figure 1. Schematic of three convection drivers in the magnetosphere and ionosphere, adapted from *Cowley* (1982) with the addition of a reconnection X-line in the cross-tail current sheet (in green, the voltage across which is Φ_N). This X-line re-closes open field lines and is included here because in the ECPC model (*Cowley and Lockwood*, 1992) it contributes to the ionospheric transpolar voltage Φ_{PC} at any one time by adding to the effect of the reconnection voltage Φ_D along the dayside magnetopause X-line (in red) which generates open field lines. The third source of Φ_{PC} is "viscous-like" momentum transfer across the magnetopause onto closed field lines that generates a total antisunward magnetic flux transfer of closed flux of voltage Φ_V in the low latitude boundary layers (LLBL).

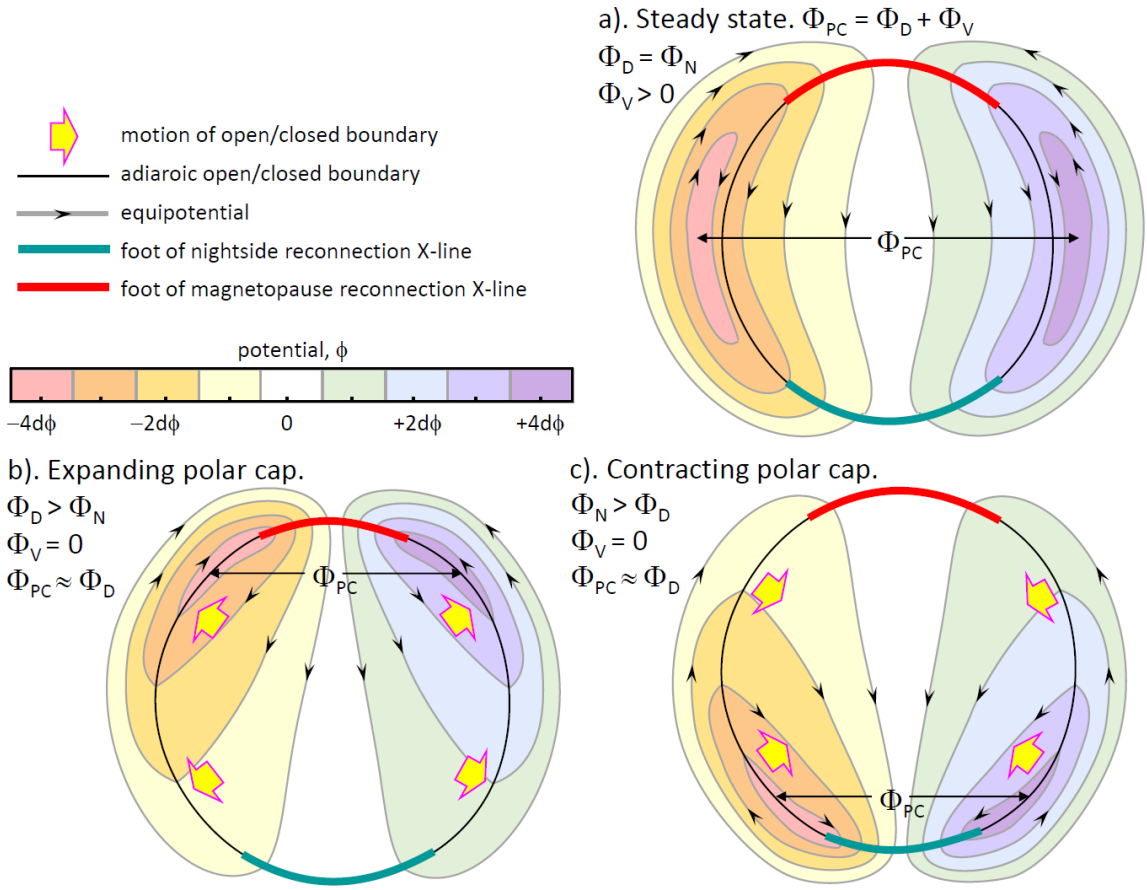

1308

1309 **Figure 2**. Schematic illustration of northern hemisphere ionospheric flow streamlines
1310 (equipotentials, $d\phi$ apart) under the influence of three driving voltages Φ_D , Φ_N and
1311 Φ_V discussed in Figure 1, as predicted by the ECPC model of ionospheric flow excitation for
1312 the special case where polar cap remains circular: (a) is for steady state (also known as
1313 balanced reconnection), (b) for an expanding polar cap and (c) for a contracting polar cap.

1314

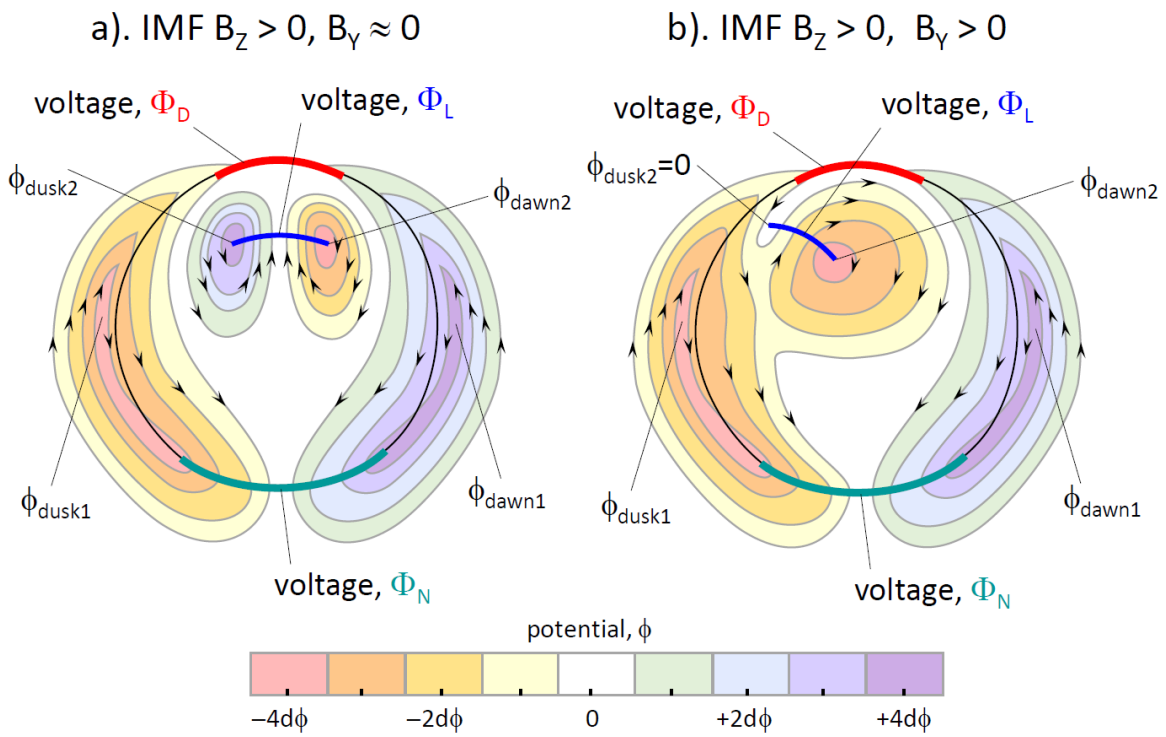

Figure 3. Schematic illustrations of northern-hemisphere ionospheric flow streamlines (equipotentials $d\phi$ apart) during northward IMF ($B_Z > 0$) and under the influence of the three driving voltages Φ_D, Φ_N and Φ_V discussed in Figure 1, plus a lobe reconnection voltage Φ_L. Both cases are for a contracting polar cap with $\Phi_N > \Phi_D$ giving poleward motion of the adiaroic polar cap boundaries. In part (a), lobe reconnection with IMF $B_Y \approx 0$ gives two symmetric lobe circulation cells in the polar cap. Part (b) is an example of a case with large IMF $|B_Y|$, showing the effect of $B_Y > 0$ in the northern hemisphere, which yields a dominant dawn lobe cell, the sunward flow portion of which can merge with main dusk cell at the lower potentials because of the poleward contraction of the dusk adiaroic polar cap boundary. In part (a) Φ_L is close to the value of Φ_{PC} that is set by Φ_D , Φ_N and Φ_V: in terms of the potential separation $d\phi$, the schematic in part (a) is for $\Phi_N = 8d\phi$, $\Phi_D = 2d\phi$, $\Phi_L = 8d\phi$ and $\Phi_V = 2d\phi$. In part (b) $\Phi_N = 8d\phi$, $\Phi_D = 2d\phi$, $\Phi_L = 4d\phi$ and $\Phi_V = 2d\phi$.

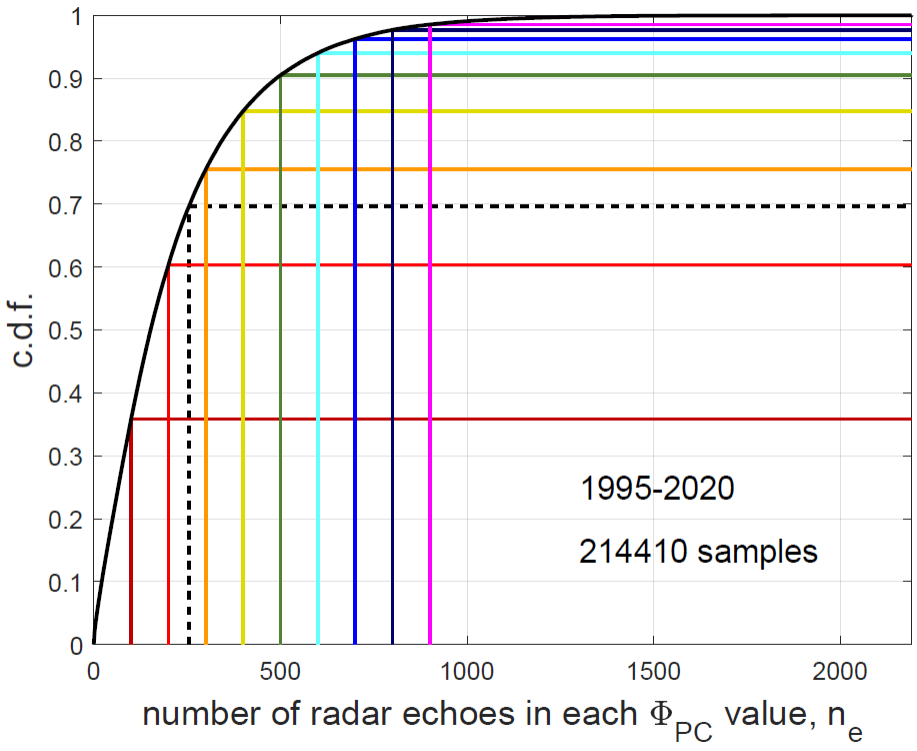

Figure 4. Cumulative probability distribution of the number of radar echoes, n_e, used in compiling the convection patterns, and hence the transpolar voltage Φ_{PC} estimates in the dataset employed here of 214410 Φ_{PC} values obtained from the SuperDARN radar array using the map-potential technique between 1995 and 2020. The vertical lines are various threshold values n_{min} used in this paper which n_e must exceed for the Φ_{PC} value obtained to be considered valid. The vertical-coloured lines are at n_{min} of [100:100:900] and the black dashed line is at 255. The condition $n_e > n_{min} = 255$ was found to be optimum in a comparison with 2-years data from satellite passes (for 2001 and 2002, see Appendix A) and which yields $N = 60653$ valid Φ_{PC} estimates which is close to 30% of all observations. The coloured thresholds are here used in a sensitivity study to understand the effect of the adopted n_{min} threshold.

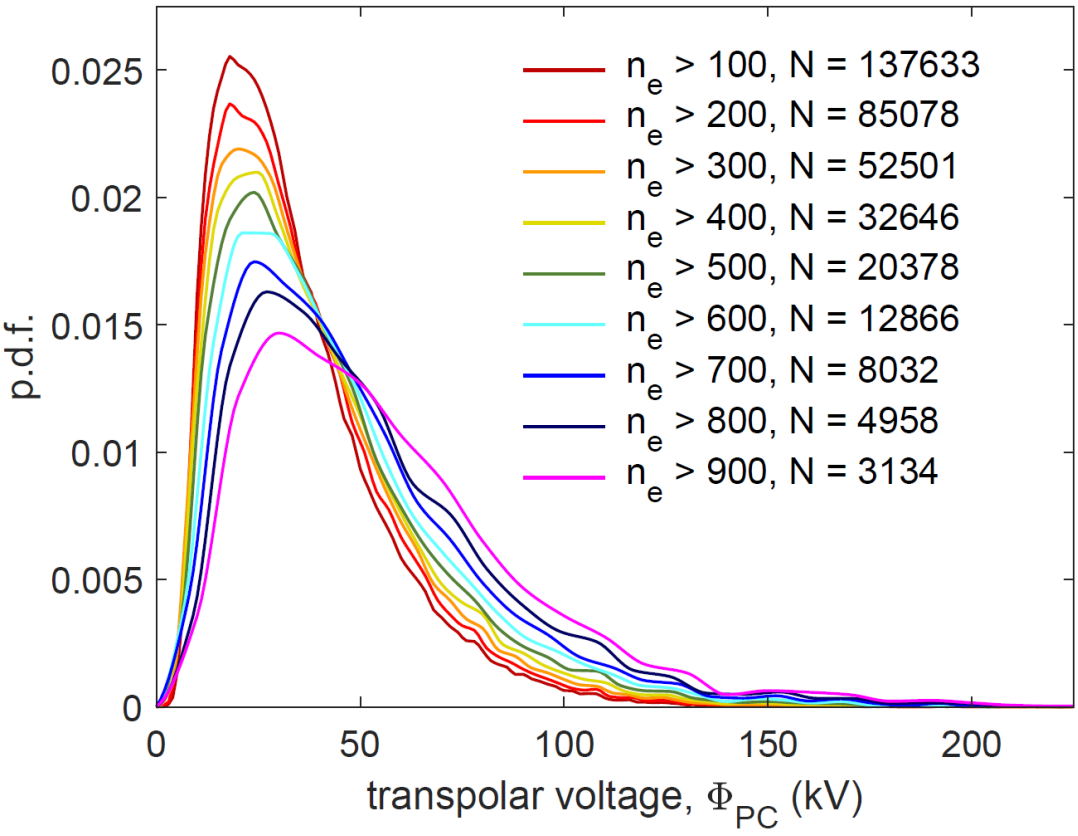

Figure 5. Probability density functions giving the normalised distributions of the Φ_{PC} values for threshold values for the number of echoes n_e required of $n_{\min} = [100{:}100{:}900]$. The resulting total number of Φ_{PC} values in the data set meeting that requirement, N, is given in each case.

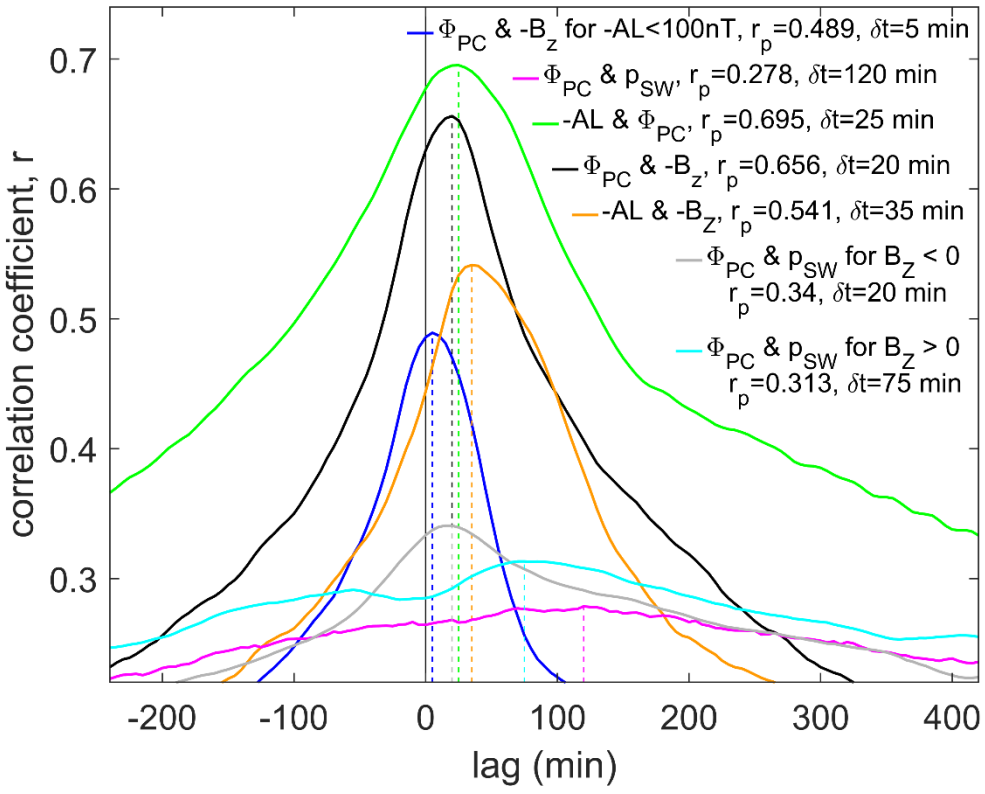

1345

1346 **Figure 6**. Lag correlograms used to determine the optimum lags δt: (black) for Φ_{PC} and IMF
1347 $-B_Z$ (in the GSM frame); (blue) for Φ_{PC} and IMF $-B_Z$ (in the GSM frame) for the subset with
1348 $-AL < 100nT$; (orange) for the $-AL$ index and IMF $-B_Z$; (green) the $-AL$ index and Φ_{PC}.
1349 The mauve, grey and cyan lines are for Φ_{PC} and the solar wind dynamic pressure p_{SW}:
1350 mauve is for all data, grey for southward IMF (B_Z < 0) and cyan for northward IMF (B_Z > 0).
1351 In each case, the first parameter of the pair has been lagged with respect to the second by the
1352 lag given by the x-axis. The vertical dashed lines are at the lag δt yielding maximum r, r_p,
1353 and the values for δt and r_p are given for each case in the legend. All data are selected by the
1354 Φ_{PC} dataset for $n_e > n_{lim} = 255$ radar echoes.

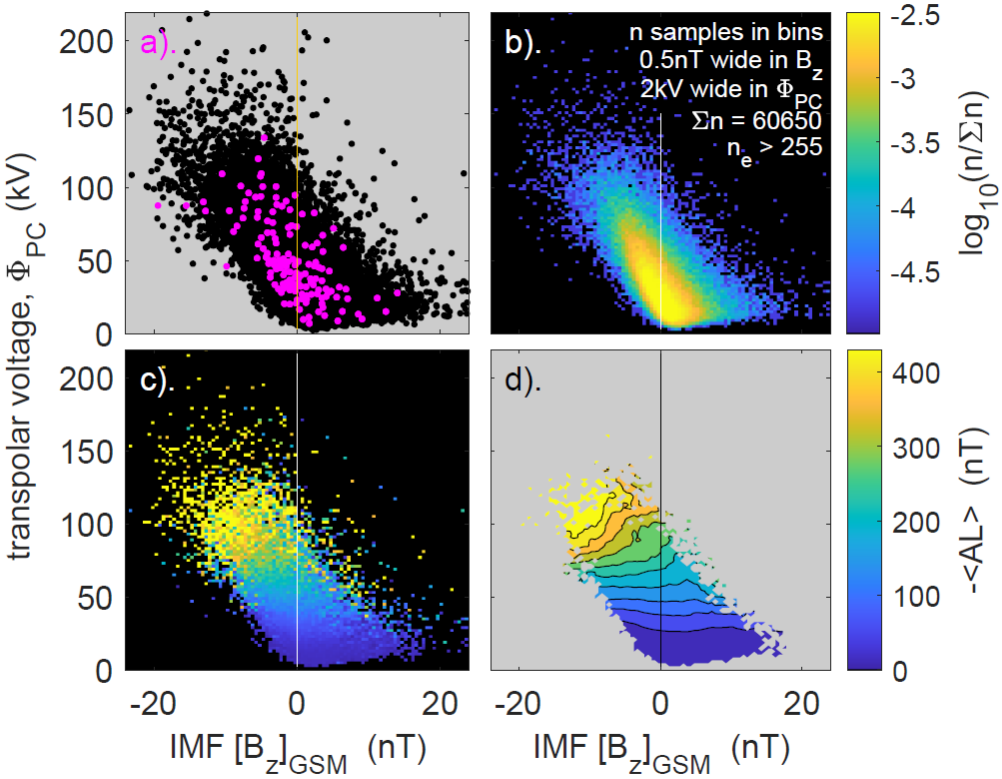

Figure 7. (a) Scatter plots of transpolar voltage estimates Φ_{PC} as a function of the IMF B_Z component. The black points are for the survey of SuperDARN presented here (for $n_e > 255$) and the mauve points are from the survey of data from various spacecraft by *Cowley* (1984). (b) The fraction of samples $n/\Sigma n$ (on a logarithmic scale) in bins that are $\Delta B_z = 0.5nT$ wide in IMF B_z (in the GSM frame of reference) and $\Delta\Phi_{PC} = 2\ kV$ wide in the Φ_{PC}, as a function of B_z and Φ_{PC}. The IMF B_z data are 15-minute boxcar running means of 1-min. observations. (c). The mean negative AL index $-< AL >$ in the same bins as used in part (b). In both panels only Φ_{PC} values based on $n_e > 255$ radar echoes are used and bins with no samples are shaded black. Part (d) shows the same data as part (c), fitted with contour levels. Note in relation to Part (a), *Cowley* (1984) presented the data in terms of the dawn-to-dusk interplanetary electric field, $E_Y = V_{SW}B_Z$ whereas we here use an *x*-axis of $B_Z = E_Y/V_{SW}$. Also the satellite Φ_{PC} data have been scaled to the radar values using the best-fit linear regression shown in part (c) of Figure A1 in Appendix A.

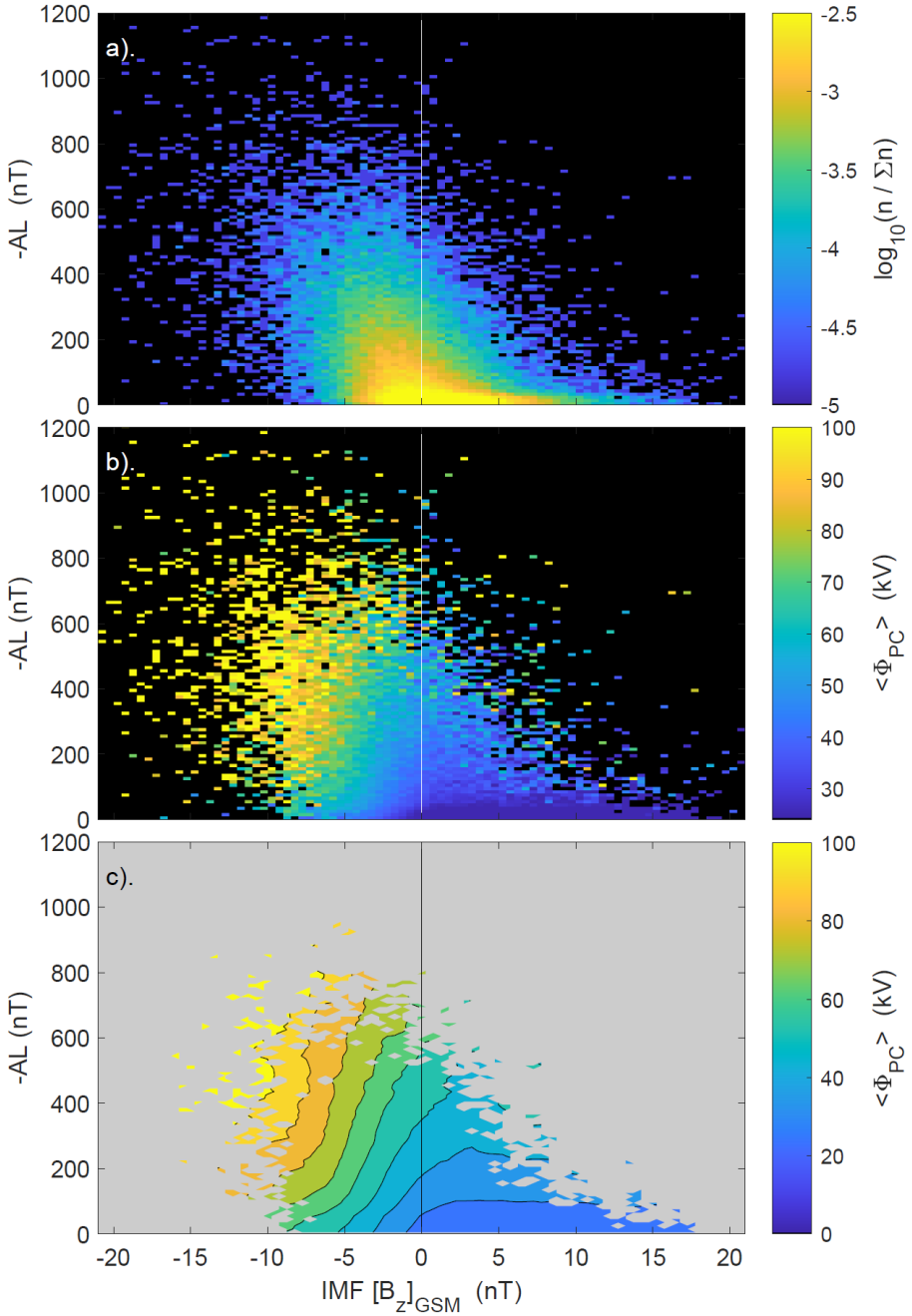

Figure 8. Plots on IMF B_z component and AL index axes of (a) the fraction of samples $n/\Sigma n$ (on a logarithmic scale) and (b) mean transpolar voltage $< \Phi_{PC} >$ in bins that are $\Delta B_z = 0.5nT$ wide in IMF B_z (in the GSM frame of reference) and $\Delta AL = 10\ nT$ wide in the AL index, as a function of B_z and $-AL$. Both of B_z and AL data are 15-minute boxcar running means of 1- minute observations. Bins with no samples are shaded black. Only Φ_{PC} values based on $n_e > 255$ radar echoes are used. Part (c) shows the same data as Part (b), fitted with contour levels.

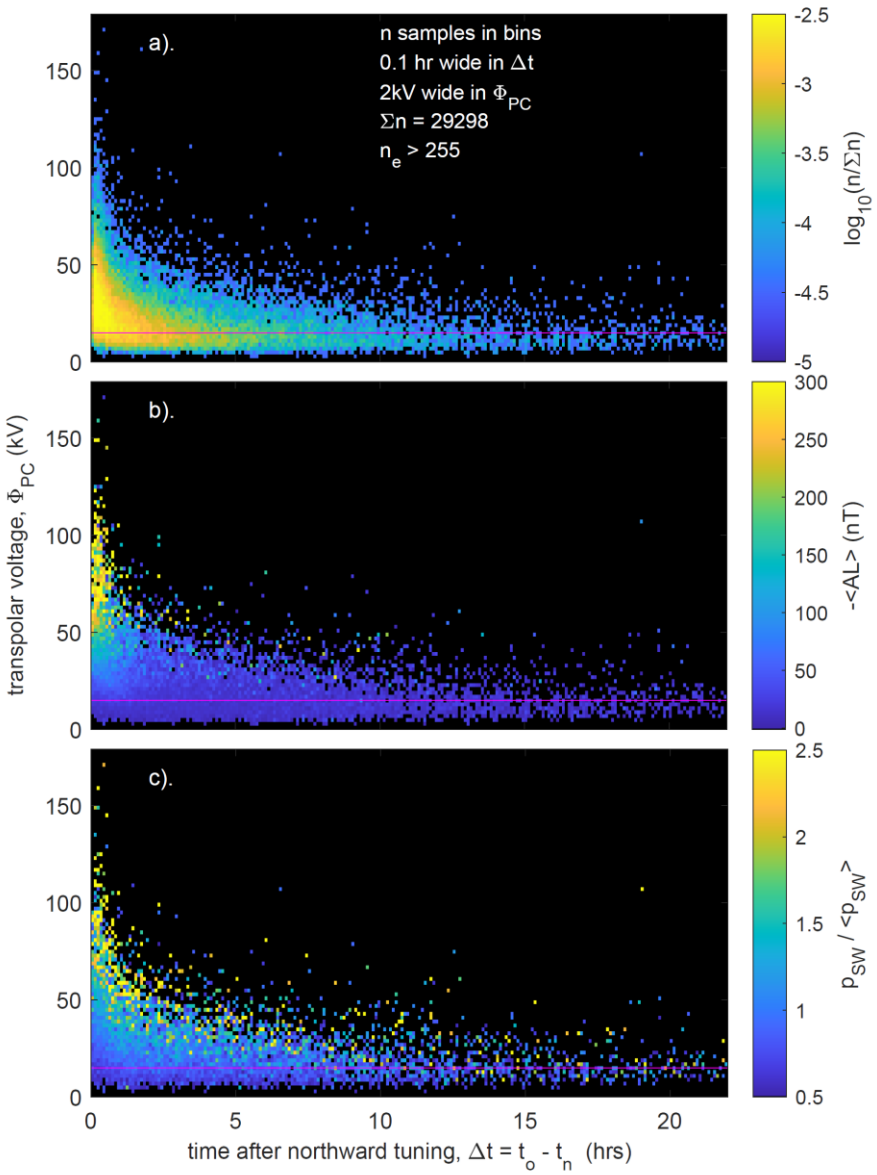

1377

1378 **Figure 9**. (a) The fraction of samples $n/\Sigma n$ (on a logarithmic scale) during continuous
1379 northward IMF ($B_z > 0$ in the GSM frame of reference, using 15-minute boxcar running
1380 means of 1-minute IMF data) as a function of Φ_{PC} and the time that the IMF has been
1381 northward, $\Delta t = (t_o - t_n)$, where t_o is the time of the Φ_{PC} observation and t_n is the time at
1382 which the IMF turned northward, in bins that are $0.1 hr$ wide in Δt and $2\ kV$ wide in Φ_{PC}.
1383 Bins with no samples are shaded black. (b) The same as (a) for the mean negative AL index
1384 $-< AL >$. (c) The same as (a) for the normalised solar wind dynamic pressure,
1385 $p_{SW}/< p_{SW} >$. In all there panels only Φ_{PC} values based on $n_e > 255$ radar echoes are used
1386 and bins with no samples are shaded black.

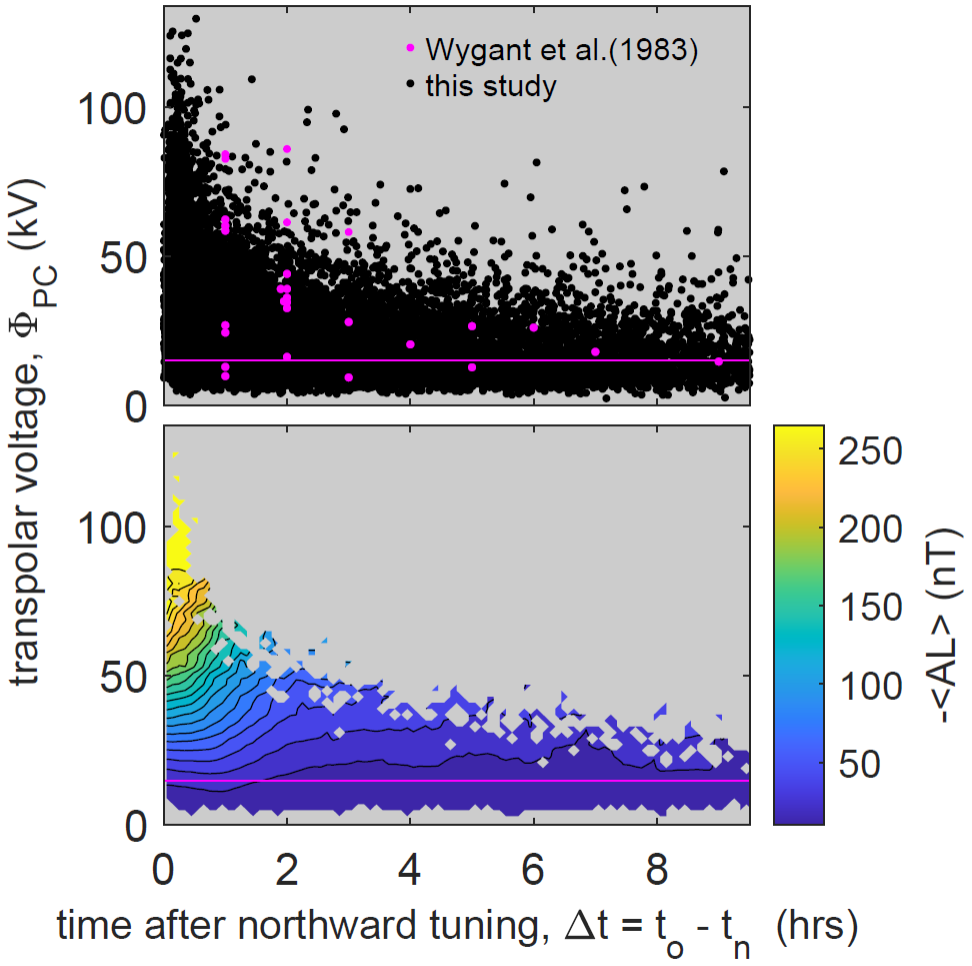

Figure 10. Detail of Figure 9 at small times since the IMF turned northward, $\Delta t = (t_o - t_n)$, where t_o is the time of the Φ_{PC} observation and t_n is the time at which the IMF turned northward. The black dots in the top panel form a scatter plot of the Φ_{PC} data as a function of Δt from the present survey. The mauve dots are the satellite Φ_{PC} data from *Wygant et al.* (1983), which have been scaled to the radar values using the best-fit linear regression shown in part (c) of Figure A1 in Appendix A. The lower panel shows contours of the mean *AL* index for the data points of the present survey (and so is a contoured version of Figure 9b for small Δt).

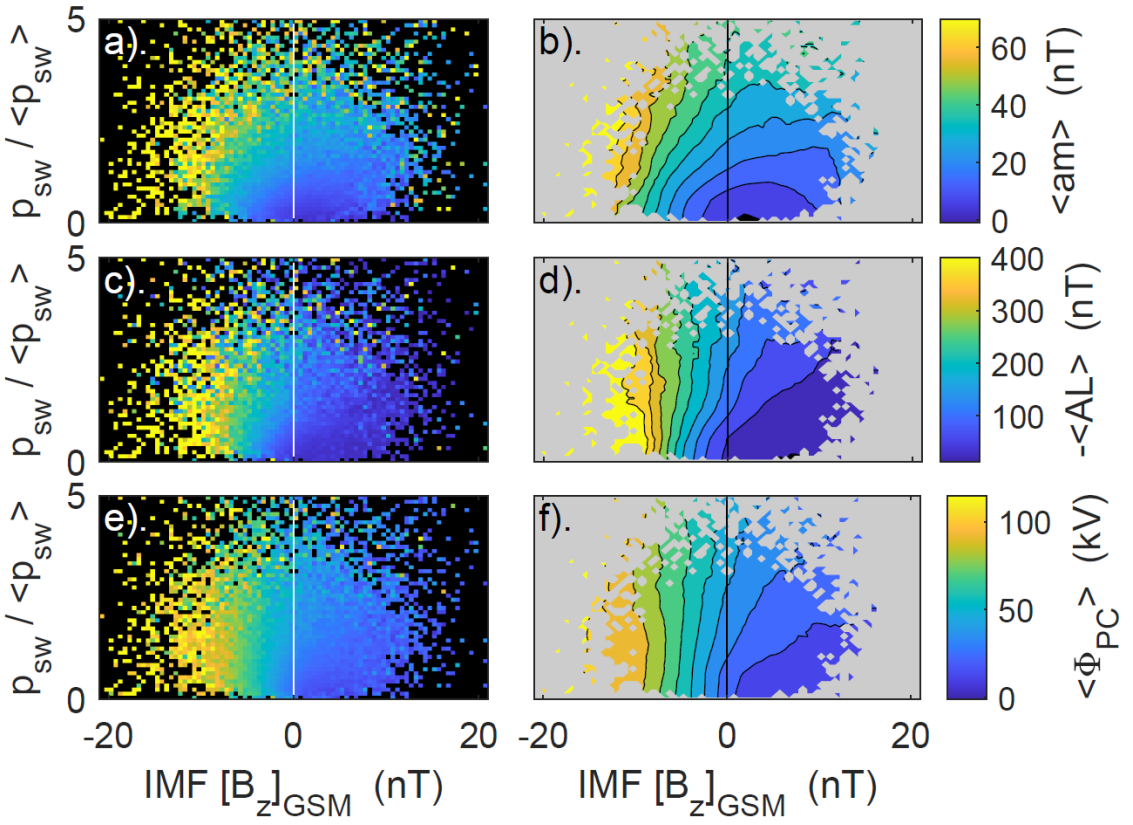

Figure 11. The left-hand plots show mean values in bins and the right-hand plots the same data fitted with contours. The top plots (a) and (b) are for the mid-latitude am geomagnetic range index; the middle plots (c) and (d) are for the mean negative AL index; and the bottom plots (e) and (f) are for the mean transpolar voltage Φ_{PC}. All are as a function of the north-south IMF component (B_z, defined as positive northward) in the GSM frame of reference and the normalised solar wind dynamic pressure, $p_{SW}/< p_{SW} >$, where $p_{SW} = m_{SW} N_{SW} V_{SW}^2$ and m_{SW} is the mean ion mass, N_{SW} the number density and V_{SW} the speed of the solar wind and the normalising factor $< p_{SW} >$ is the mean for all data in the 1995-2020 period of this study. The AL, Φ_{PC}, and p_{SW} are all 15-minute boxcar running means of 1-minute data whereas the am data are linearly interpolated to the time of the Φ_{PC} sample from the raw 3-hourly am data. Bins are $\Delta B_z = 0.5nT$ wide in IMF B_z and 0.1 wide in $p_{SW}/< p_{SW} >$. Bins with no samples are shaded black in the left-hand panels and give areas of gey on the right where the data are too sparse for contours to be fitted. The am, $-AL$, and Φ_{PC} values used were for times of Φ_{PC} samples that are based on $n_e > 255$ radar echoes.

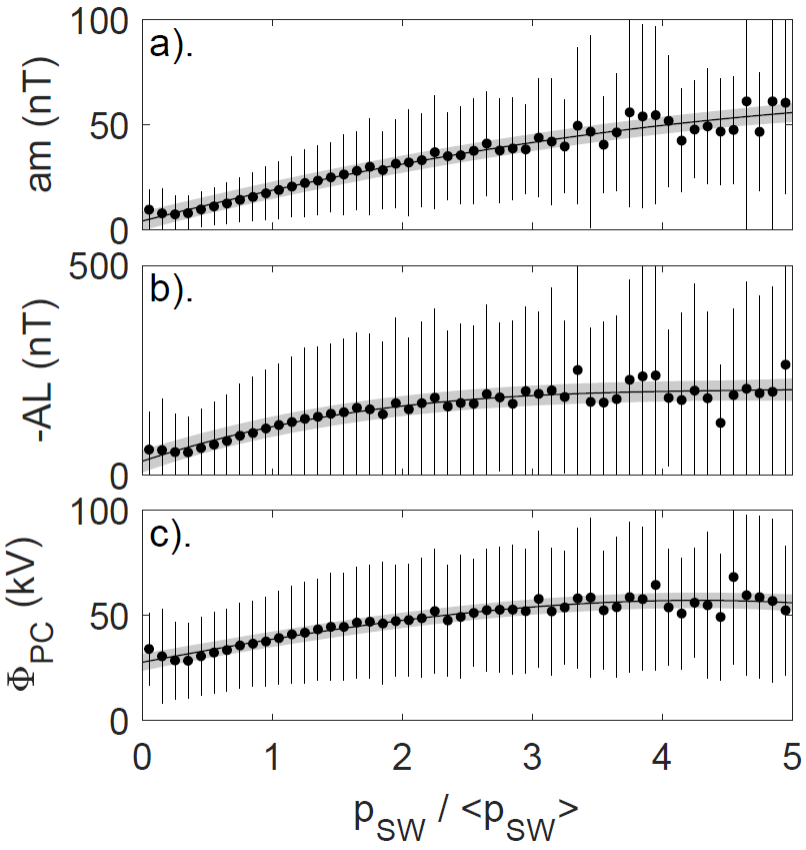

Figure 12. Mean values (with uncertainty bars of plus and minus one standard deviation) of (a) the am geomagnetic range index, (b) the negative AL index and (c) the transpolar voltage Φ_{PC} as a function of the normalised solar wind dynamic pressure $p_{SW}/< p_{SW} >$ in bins that are 0.1 wide in $p_{SW}/< p_{SW} >$. The black line is the best 3rd-order polynomial fit to the mean values and the grey area around it is bound by plus and minus the 1-sigma error in the fit. The am, $-AL$, and Φ_{PC} values used were for times of Φ_{PC} samples that are based on $n_e >$ 255 radar echoes.

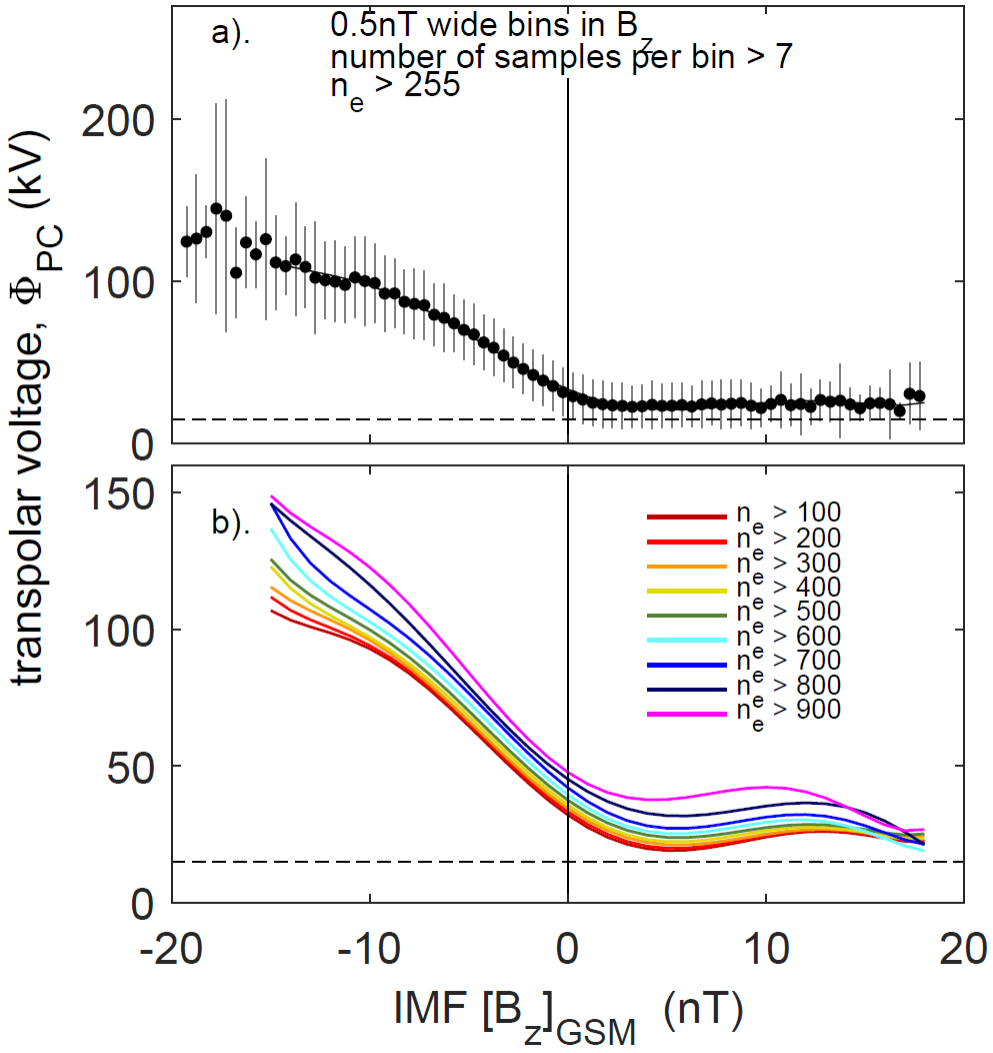

1419

1420 **Figure 13**. (a) Mean values (with uncertainty bars of plus and minus one standard deviation)
1421 of the transpolar voltage Φ_{PC} as a function of IMF B_z (in the GSM frame of reference) in bins
1422 that are $\Delta B_z = 0.5nT$ wide for Φ_{PC} samples that are based on $n_e > 255$ radar echoes. The
1423 solid line is a 6th-order polynomial fit to the mean values. (b). Analysis of the effect on part
1424 (a) of the threshold required for the number of radar echoes, n_e. The coloured lines are 6th-
1425 order polynomial fits to the mean values of Φ_{PC} for n_e thresholds of n_{lim} = [100:100:900]
1426 that were also used in Figures 4 and 5.

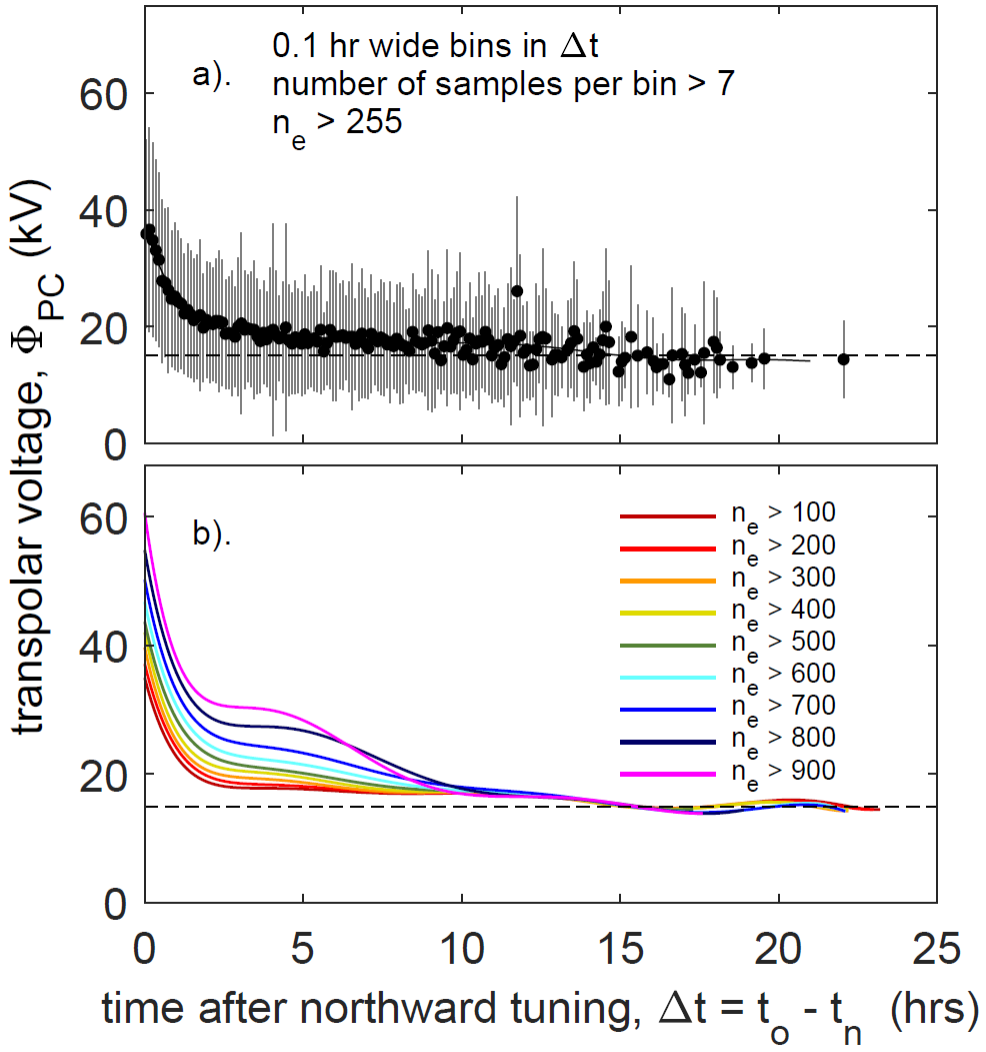

1427

1428 **Figure 14**. (a) Mean values (with uncertainty bars of plus and minus one standard deviation)
1429 of the transpolar voltage Φ_{PC} during northward IMF as a function of time since the IMF
1430 turned northward, $\Delta t = (t_o - t_n)$ in bins that are $0.1hr$ wide: t_o is the time of the Φ_{PC}
1431 observation and t_n is the time at which the IMF turned northward. Φ_{PC} samples are based on
1432 $n_e > 255$ radar echoes. The solid line is a 6th-order polynomial fit to the mean values. (b)
1433 Analysis of the effect on part (a) of the threshold required for the number of radar echoes, n_e.
1434 The coloured lines are 6th-order polynomial fits to the mean values of Φ_{PC} for n_e thresholds
1435 of [100:100:900] that were also used in Figures 4, 5 and 13.

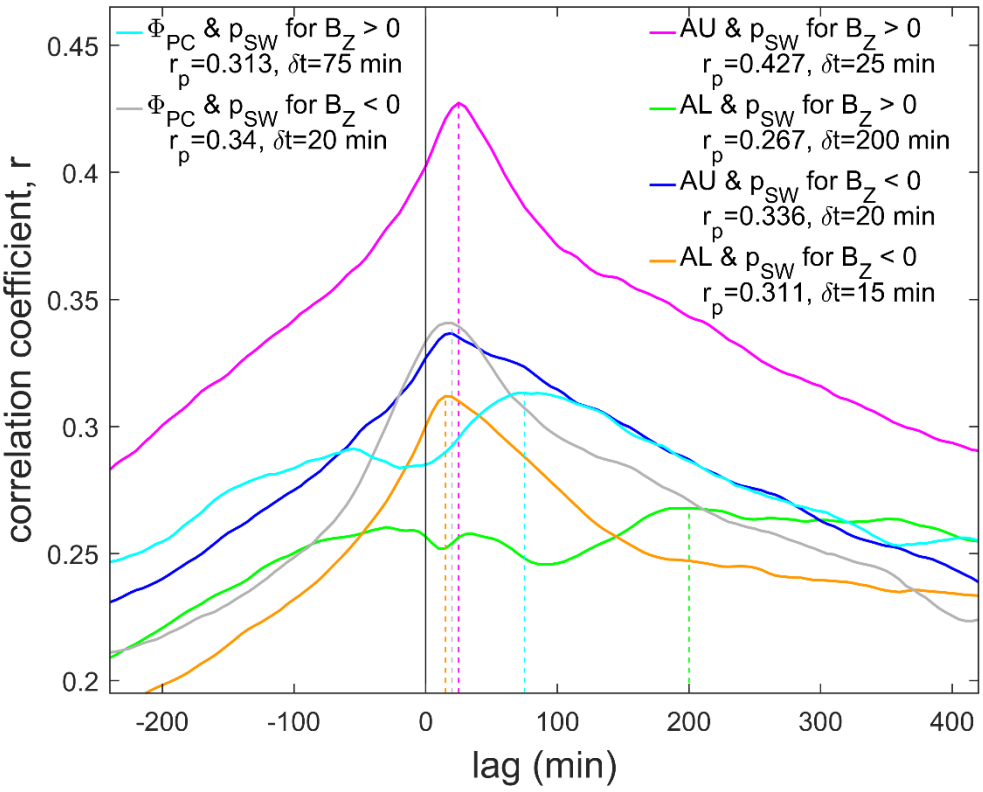

Figure 15. Lag correlograms for auroral electrojet indices with solar wind dynamic pressure: (mauve) for AU and p_{SW} for IMF $B_Z > 0$ (in the GSM frame); (green) for AL and p_{SW} for IMF $B_Z > 0$; (blue) for AU and p_{SW} for IMF $B_Z < 0$; and (orange) for AL and p_{SW} for IMF $B_Z < 0$. In each case, the first parameter of the pair has been lagged with respect to the second by the lag given by the x-axis. The vertical dashed lines are at the lag δt yielding maximum r, r_p, and the values for δt and r_p are given for each case. The cyan and grey lines are the corresponding lag correlograms for the transpolar voltage Φ_{PC} and p_{SW} for IMF $B_Z > 0$ and IMF $B_Z < 0$, respectively.

Appendix A.

The SuperDARN data used here were processed at the Institute of Space and Atmospheric Studies, University of Saskatchewan, using the SuperDARN Radar Software Toolkit (RST) 4.3 (2019) developed and maintained by the SuperDARN Data Analysis Working Group and available from the Github URL https://zenodo.org/record/3401622#.YNuIbUwo-1k

SuperDARN Data Analysis Working Group. Participating members; Thomas, E. G.; Sterne, K. T.; Shepherd, S. G.; Kotyk, K.; Schmidt, M. T.; Ponomarenko, P. V.; Bland, E. C.; Walach, M.-T.; Reimer, A. S.; Burrell, A. G.; Billett, D. D. (2019) SuperDARN Radar Software Toolkit (RST) 4.3, doi: 10.5281/zenodo.3401622

To allow reproduction of the dataset, note that all the RST (version 4.3) defaults were used to create the potential maps, except the following:

(i) fitacf-version 3.0 was used instead of fitacf-version 2.5

(ii) -tl 60 (scan time 60 seconds)

(iii) -c (concatenate grid files)

(iv) -minrng 10 (include data from minimum range gate 10)

(v) use -cn a, b, c, d for channel fitacf files (a, b, c, d in the filename), or -cn_fic A, b for fitacfs with twofsound for channel 0 and 1 for A and channel 2 for B

(vi) -xtd for extra variable spectral width and SNR

(vii) -stime 00:00 to give start time at 00:00

(vii) -vemax 10000 to exclude any data above velocity value of 10,000 ms^{-1}

(viii) -l 50 to set map minimum latitude to 50 degrees

(ix) -if OMNI.txt to use OMNI dataset to drive re-analysis model

(x) -d 00:10 for 10 minute delay on the input OMNI data. Note that the results were not sensitive to this value and Figure 6 of the main paper shows that the observed lag between Φ_{PC} and IMF B_z is 20 min and set by the observed radar Doppler shifts and not the model.

(xi) -o 8 for harmonic order 8

(xii) -d l for low doping level. The doping level sets the relative weight given to the model compared to the data and can be set to light, medium and heavy. As we wish the maps to be strongly data-driven, we have set the model doping to light.

We here present an overview plot of the comparisons between SuperDARN and DMSP transpolar voltages (respectively $[\Phi_{PC}]_{\text{S.DARN}}$ and $[\Phi_{PC}]_{\text{DMSP}}$) referred to in the text. (The full analysis will appear in the paper Lockwood, M., K.A. McWilliams, and M.R. Hairston, Semiannual and Universal Time variations in magnetospheric convection: 1. Transpolar Voltage Data, to be submitted to J. Geophys. Res.). These comparisons are for data from 2001 and 2002 and are for dawn-to-dusk DMSP passes only and consider the effects of both the proximity of the satellite path the diameter of the polar cap giving the transpolar voltage in the SuperDARN data (quantified by the parameter δ_{max}) and the number of echoes, n_e involved in computing $[\Phi_{PC}]_{\text{S.DARN}}$.

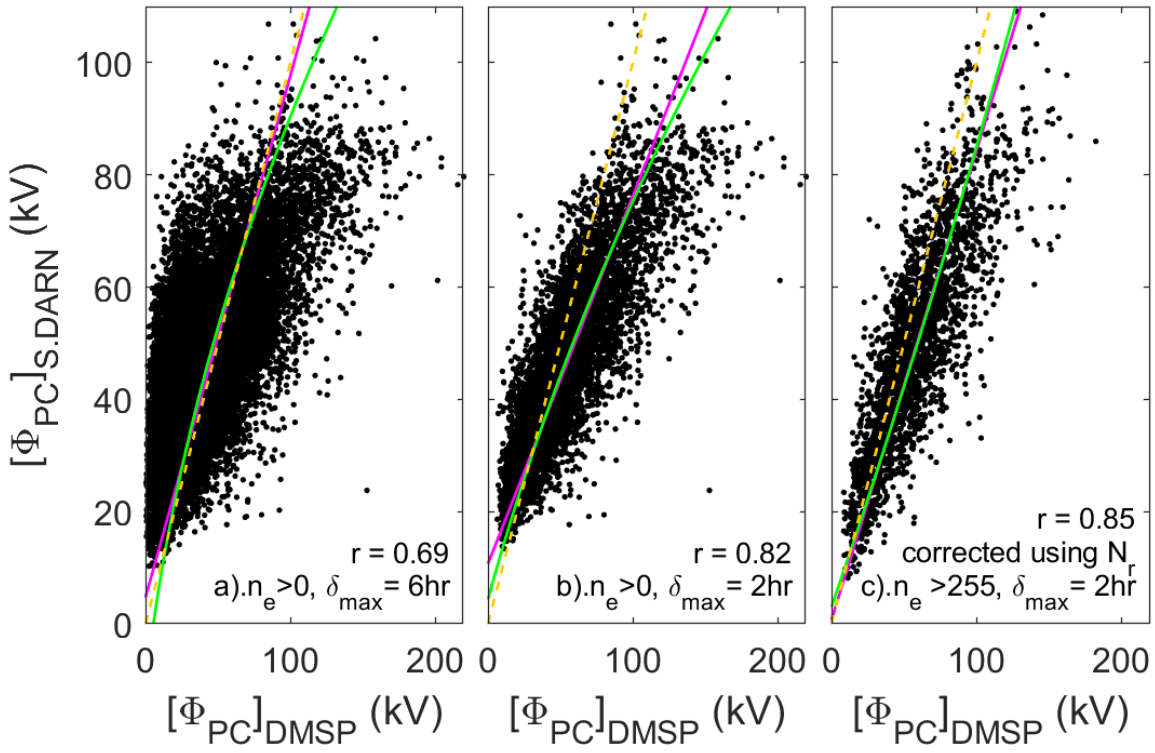

Figure A1. Comparisons of simultaneous (with 30 minutes) transpolar voltage measurements by the SuperDARN radars, $[\Phi_{PC}]_{S.DARN}$, and from DMSP satellite passes, $[\Phi_{PC}]_{DMSP}$. The scatter plot in (a) is for all data, irrespective of how many radar Doppler shift measurements contributed to the SuperDARN values and the Magnetic Local Times (δ values) of the DMSP intersections of the convection reversal boundary (CRB). In (b) the derived stringent criterion for the MLT of the DMSP intersections of the CRB ($\delta \leq \delta_{max} = 2hrs$) has been applied. In (c) The same restriction is applied to the DMSP passes and the number of radar data points, n_e must exceed 255. On all three plots, the mauve line is the best linear regression, the green line the 2nd-order polynomial fit, and the orange dashed line the ideal agreement ($[\Phi_{PC}]_{S.DARN} = [\Phi_{PC}]_{DMSP}$). The correlation coefficient, r, and the r.m.s. deviation of the two data sets, Δ, is given in each case. The number of data points in (a), (b) and (c) are 16714, 6023 and 2468, respectively.